bioRxiv preprint doi: https://doi.org/10.1101/353490; this version posted June 22, 2018. The copyright holder for this preprint (which was not certified by peer review) is the author/funder, who has granted bioRxiv a license to display the preprint in perpetuity. It is made available under aCC-BY 4.0 International license.

Hair Follicle Epidermal Stem Cells Define a Niche for Tactile Sensation

Chun-Chun Cheng[1,9,11], Ko Tsutsui[1,11], Toru Taguchi[2,10,11], Noriko Sanzen[1], Asako Nakagawa[1], Kisa Kakiguchi[3], Shigenobu Yonemura[3,4], Chiharu Tanegashima[5], Sean D. Keeley[5], Hiroshi Kiyonari[6], Yasuhide Furuta[6], Yasuko Tomono[7], Fiona M. Watt[8] and Hironobu Fujiwara[1,*]

[1]Laboratory for Tissue Microenvironment, RIKEN Center for Biosystems Dynamics Research (BDR), Kobe 650-0047, Japan

[2]Department of Neuroscience II, Research Institute of Environmental Medicine, Nagoya University, Nagoya 464-8601, Japan

[3]Ultrastructural Research Team, Center for Biosystems Dynamics Research (BDR), Kobe 650-0047, Japan

[4]Department of Cell Biology, Tokushima University Graduate School of Medical Science, Tokushima 770-8503, Japan

[5]Phyloinformatics Unit, Center for Biosystems Dynamics Research (BDR), Kobe 650-0047, Japan

[6]Animal Resource Development Unit and Genetic Engineering Team, Center for Biosystems Dynamics Research (BDR), Kobe 650-0047, Japan

[7]Division of Molecular & Cell Biology, Shigei Medical Research Institute, Okayama 701-0202, Japan

[8]Centre for Stem Cells and Regenerative Medicine, King's College London, London SE1 9RT, UK

[9]Present address: Simmons Comprehensive Cancer Center, UT Southwestern Medical Center, Texas 75390, USA

bioRxiv preprint doi: https://doi.org/10.1101/353490; this version posted June 22, 2018. The copyright holder for this preprint (which was not certified by peer review) is the author/funder, who has granted bioRxiv a license to display the preprint in perpetuity. It is made available under aCC-BY 4.0 International license.

[10]Present address: Department of Physical Therapy, Niigata University of Health and Welfare, Niigata 950-3198, Japan

[11]Co-first author

*Correspondence: hironobu.fujiwara@riken.jp

bioRxiv preprint doi: https://doi.org/10.1101/353490; this version posted June 22, 2018. The copyright holder for this preprint (which was not certified by peer review) is the author/funder, who has granted bioRxiv a license to display the preprint in perpetuity. It is made available under aCC-BY 4.0 International license.

Abstract

The heterogeneity and compartmentalization of stem cells is a common principle in many epithelia, and is known to function in epithelial maintenance, but its other physiological roles remain elusive. Here we show transcriptional and anatomical contributions of compartmentalized epidermal stem cells (EpSCs) in tactile sensory unit formation in the hair follicle (HF). EpSCs in the follicle upper-bulge, where mechanosensory lanceolate complexes (LCs) innervate, express a unique set of extracellular matrix (ECM) and neurogenesis-related genes. These EpSCs deposit an ECM protein EGFL6 into the collar matrix, a novel ECM that tightly ensheathes LCs. EGFL6 is required for the proper patterning, touch responses, and αv integrin-enrichment of LCs. By maintaining a quiescent original EpSC niche, the old bulge, EpSCs provide anatomically stable HF–LC interfaces, irrespective of the stage of follicle regeneration cycle. Thus, compartmentalized EpSCs provide a niche linking the HF and the nervous system throughout the hair cycle.

bioRxiv preprint doi: https://doi.org/10.1101/353490; this version posted June 22, 2018. The copyright holder for this preprint (which was not certified by peer review) is the author/funder, who has granted bioRxiv a license to display the preprint in perpetuity. It is made available under aCC-BY 4.0 International license.

Introduction

Tissue stem cells (SCs) in many epithelia, including the epidermis, intestine, mammary glands and lungs, often comprise heterogeneous populations with distinct transcriptional and anatomical features (Donati & Watt, 2015; Xin, Greco, & Myung, 2016). Individual SC pools contribute to tissue maintenance through different homeostatic and regenerative properties and give rise to distinct epithelial compartments, while they also hold plasticity to change their identity and function when perturbed. These recent findings question the traditional view of the role of stem cell heterogeneity, which underlies the theory of linear hierarchy (Goodell, Nguyen, & Shroyer, 2015). Although the biological significance of the heterogeneity and compartmentalization of epithelial SCs has primarily been studied in the context of epithelial tissue maintenance and regeneration, its other physiological roles remain unclear.

Hair follicles (HFs) are highly conserved touch sensory organs in the hairy skin that covers most of the mammalian body surface and detects touch signals essential for development and survival (Lumpkin, Marshall, & Nelson, 2010). HFs are innervated by mechanosensory end organs called lanceolate complexes (LCs), which are composed of parallel, longitudinally aligned low-threshold mechanoreceptor (LTMR) axonal endings and terminal Schwann cell (tSC) processes (Zimmerman, Bai, & Ginty, 2014). HFs are also connected to arrector pili muscles (APMs), thus forming a unique regenerating motile sensory organ. These two HF appendages attach to the permanent portion of the HF, known as the bulge, where epidermal stem cells (EpSCs) reside.

Hair follicle EpSCs are heterogeneous in their molecular and functional properties and compartmentalized along the longitudinal axis of the HF (Figure 1A) (Solanas & Benitah, 2013). The mid-bulge region contains $CD34^{+}$ slow-cycling EpSCs that serve as a reservoir of EpSCs and were once thought to be the master SCs at the top of the epidermal

bioRxiv preprint doi: https://doi.org/10.1101/353490; this version posted June 22, 2018. The copyright holder for this preprint (which was not certified by peer review) is the author/funder, who has granted bioRxiv a license to display the preprint in perpetuity. It is made available under aCC-BY 4.0 International license.

hierarchy. A series of recent studies, however, identify several additional pools of different EpSCs around the bulge (e.g. in the isthmus, junctional zone, upper-bulge and hair germ). For example, the upper-bulge is a niche for *Gli1*$^{+}$ EpSCs and they contribute to HF regeneration and wound healing of interfollicular epidermis (Brownell, Guevara, Bai, Loomis, & Joyner, 2011). The importance of EpSC heterogeneity and compartmentalization has almost entirely been explained by their role in regional tissue replenishment to maintain different functional compartments of the epidermis, but its roles apart from epidermal maintenance remain poorly understood. As coordinated epithelial–mesenchymal interactions are essential for HF development, regeneration and functioning, the unique signaling territories and tissue architecture provided by compartmentalized EpSCs probably regulate the interactions between the epidermis and a variety of HF-associated structures, including sensory nerves, APMs and the dermal papilla. Consistent with this idea, it has been reported that mid-bulge EpSCs create a specialized basement membrane containing nephronectin, thereby providing a niche for APM development and anchorage (Fujiwara et al., 2011). Follicle epidermis-derived BDNF is also critical for follicle-nerve interactions (Rutlin et al., 2014).

In this study, we set out to address the idea that upper-bulge EpSCs are molecularly and anatomically specialized for interaction with LCs and thus involved in generating the sense of touch. We demonstrated that upper-bulge EpSCs produce a special extracellular matrix (ECM) environment and unique epidermal tissue architecture that creates a stable HF–LC interface for tactile sensation. Thus, EpSC heterogeneity and compartmentalization appear to be important for both regional epidermal maintenance and patterned epithelial–mesenchymal interactions.

bioRxiv preprint doi: https://doi.org/10.1101/353490; this version posted June 22, 2018. The copyright holder for this preprint (which was not certified by peer review) is the author/funder, who has granted bioRxiv a license to display the preprint in perpetuity. It is made available under aCC-BY 4.0 International license.

Results

Upper-bulge EpSCs are molecularly specialized for HF–nerve interactions

We first examined the global transcriptional features of distinct EpSC populations in the HF. To this end, we established FACS-based cell purification methods using several eGFP reporter mouse lines that label different SC compartments to isolate cellular subpopulations resident in the lower-isthmus (*Lgr6*$^+$), upper-bulge (*Gli1*$^+$), mid-bulge (CD34$^+$), and hair germ (*Cdh3*$^+$) as well as unfractionated basal EpSCs (α6 integrin$^+$) (Figure 1A and B, Figure 1–figure supplement 1A). The purity of the isolated populations was verified by the expression of compartment-specific genes (Figure 1–figure supplement 1B and C, Materials and methods). We performed RNA-seq on these isolated cell populations. Gene Set Enrichment Analysis (GSEA) indicated that neurogenesis-related Gene Ontology (GO) terms are over-represented in *Gli1*$^+$ upper-bulge EpSCs (Figure 1C, Figure 1– table supplement 1). To further identify *Gli1*$^+$ compartment–enriched genes, we performed a pairwise transcriptional comparison between the *Gli1*$^+$ population and all the other populations and plotted the relationship between *Gli1*$^+$-enriched gene sets in a Venn diagram (Figure 1D). Genes categorized in "Group I" were *Gli1*$^+$ population-enriched genes. We also extracted genes included in "Group II", which contains genes highly expressed both in the *Gli1*$^+$ population and the CD34$^+$ population, since the *Gli1* and CD34 double-positive cells were included in the CD34$^+$ population in our sorting scheme (Figure 1D). Prominent gene-annotation clusters in both Group I and Group II cells encode proteins involved in nervous system development, including the neurotrophic factors *Grp*, *Bdnf* and *Nrtn* and the keratitis-ichthyosis-deafness syndrome gene *Gjb2* (Figure 1E and F). Multiple ECM genes are also upregulated in the upper-bulge compartment, including *Aspn*, *Crispld1*, *Egfl6*, and the deafness-related ECM genes *Col4a3* and *Col4a4* (Mochizuki et al., 1994) (Figure 1E and F). This global gene expression profiling of compartmentalized EpSCs

bioRxiv preprint doi: https://doi.org/10.1101/353490; this version posted June 22, 2018. The copyright holder for this preprint (which was not certified by peer review) is the author/funder, who has granted bioRxiv a license to display the preprint in perpetuity. It is made available under aCC-BY 4.0 International license.

suggests that upper-bulge EpSCs are specialized both to interact with the nervous system and to express a unique set of ECM genes.

Upper-bulge EpSCs deposit EGFL6 into the collar matrix

It has been suggested that the ECM plays important roles in mammalian touch end organs, but the molecular identity and functions of this putative ultrastructure remain unknown (Lumpkin et al., 2010; Zimmerman et al., 2014). On examining the tissue localization of 15 upper-bulge ECM proteins, we found that 8 ECM proteins were deposited in the upper-bulge (Figure 2A, Figure 2–table supplement 1). Among them, EGFL6 exhibited the most restricted localization in the upper-bulge of all types of dorsal HFs and showed a unique C-shaped pattern with a gap at the rostral side of the HF (Figure 2B). βIII-tubulin staining showed that skin nerve endings terminate at the EGFL6 deposition sites (Figure 2B). Magnified 3D images revealed the close association of EGFL6 with longitudinal lanceolate parallel LTMR axonal endings of LCs, which are activated by tactile stimuli (Figure 2C) (Bai et al., 2015), and longitudinal processes of nestin-positive non-myelinating tSCs of LCs (Figure 2D). A close anatomical association of follicle EGFL6 with blood vessels has been reported (Xiao et al., 2013), but their direct contact was not observed (Figure 2E). To detect cells expressing *Egfl6* mRNA, we generated *Egfl6-H2b-Egfp* reporter mice. eGFP protein expression was enriched in upper-bulge EpSCs at the caudal side of the HF, but was not detected in dermal cells around the upper-bulge or dorsal root ganglia neurons that innervate to the upper bulge (Figure 2F and G).

To investigate the ultrastructural localization of EGFL6, we performed electron microscopic analysis of transverse sections of the upper-bulge. As described by Li and Ginty (2014), each LTMR axonal ending was sandwiched by processes of tSCs (Figure 2H). We identified an electron-dense amorphous ECM structure surrounding the LCs (black

bioRxiv preprint doi: https://doi.org/10.1101/353490; this version posted June 22, 2018. The copyright holder for this preprint (which was not certified by peer review) is the author/funder, who has granted bioRxiv a license to display the preprint in perpetuity. It is made available under aCC-BY 4.0 International license.

arrowheads in Figure 2H). We named this novel structure the 'collar matrix', as it tightly ensheathes the LCs. tSC processes have two openings, at the follicular basement membrane and at the opposite side of the cell, thus exposing axonal endings and tSC processes to at least two different ECMs, the HF basement membrane and the collar matrix. Although EGFL6 is expressed by the upper-bulge EpSCs, an immunogold-labeled EGFL6 antibody was detected exclusively in the collar matrix (Figure 2I), indicating that upper-bulge EpSCs secrete EGFL6, which is incorporated in the collar matrix that ensheathes LCs (Figure 2J).

EGFL6 mediates cell adhesion via αv integrins

α8β1 integrin is the only reported cell adhesion receptor of EGFL6 (Osada et al., 2005), but its expression was not detected in LCs (data not shown). To explore other cell adhesion receptors for EGFL6, we purified recombinant EGFL6 protein and performed cell adhesion assays using nine cell lines. Of these, two glial and one skin fibroblast cell lines adhered to EGFL6, whereas other cell types, including keratinocytes, did not (Figure 2–figure supplement 1A and B), suggesting that although EGFL6 is derived from the upper-bulge EpSCs, these SCs are incapable of interacting with EGFL6, rather dermal cell lineages interact and adhere to EGFL6. A point mutation into the Arg-Gly-Asp (RGD) integrin recognition sequence of EGFL6 (RGE mutant) significantly reduced its cell adhesive ability (Figure 2–figure supplement 1C). Cell adhesion to EGFL6 was inhibited by the αv integrin antibody, but not by the β1 integrin antibody (Figure 2–figure supplement 1D). Consistent with these results, αv integrin accumulated in LCs and colocalized with EGFL6 (Figure 2–figure supplement 1E). Deletion of EGFL6 decreased αv integrin and impaired its accumulation (Figure 2–figure supplement 1E and F). Together, these results demonstrate that EGFL6 induces cell adhesion via αv integrins that accumulate in the LCs in an EGFL6-dependent manner.

bioRxiv preprint doi: https://doi.org/10.1101/353490; this version posted June 22, 2018. The copyright holder for this preprint (which was not certified by peer review) is the author/funder, who has granted bioRxiv a license to display the preprint in perpetuity. It is made available under aCC-BY 4.0 International license.

EGFL6 is required for the proper patterning and touch responses of LCs

One of the central roles of the specialized ECM around neural structures, such as the perineuronal nets, is to provide adhesive and non-adhesive physical structures to support cells and therefore determine their shape and functions (Mouw, Ou, & Weaver, 2014). Thus, we next examined the effect of deleting EGFL6 on LC structures in zigzag HFs, which are the most common HF type in rodent skin and innervated by Aδ- and C-LTMRs (Li et al., 2011). *Egfl6* knockout mice showed misaligned and overlapping structures of axonal endings and tSC processes (Figure 3A and B). Quantitative 3D histomorphometrical analysis of LTMRs and tSCs revealed the significant increase of overlapping points of axons and tSC protrusions in *Egfl6* knockout mice (Figure 3A–C). The numbers and lengths of axonal endings were unchanged (Figure 3–figure supplement 1A and B). In *Egfl6* knockout tissue, the length, but not the width, of tSC processes was reduced (Figure 3–figure supplement 1C and D). *Egfl6* knockout mice did not show defects in the hair cycle (Figure 3–figure supplement 1E and F). We conclude that EGFL6 is required for proper parallel patterning of LCs.

To determine whether EGFL6 is involved in mechanotransduction, we generated skin–nerve preparations and performed a single-nerve electrophysiological analysis of Aδ-LTMRs, which are the most sensitive HF-associated LTMRs, stimulated by gentle touch and hair deflection (Bai et al., 2015; Rutlin et al., 2014; Zimmermann et al., 2009). Although the electrical responsiveness of Aδ-LTMRs in *Egfl6* knockout skin remained intact (Figure 3–table supplement 1), these receptors showed clear defects in mechanical responses. The median mechanical response threshold of Aδ-LTMRs measured using von Frey hairs was significantly higher in knockout skin (Figure 3D). To more quantitatively analyze the mechanical sensitivity of these fibers, a light touch stimulus was applied using a piezo-

bioRxiv preprint doi: https://doi.org/10.1101/353490; this version posted June 22, 2018. The copyright holder for this preprint (which was not certified by peer review) is the author/funder, who has granted bioRxiv a license to display the preprint in perpetuity. It is made available under aCC-BY 4.0 International license.

195 controlled micromanipulator (Figure 3–figure supplement 2A). Averaged touch response
196 patterns showed that knockout skin exhibits fewer action potentials than wild-type skin at
197 displacements of >32 μm (Figures 3E, Figure 3–figure supplement 2B and C). The median
198 threshold displacement of Aδ-LTMRs was about three-times higher in the knockout (Figure
199 3F). Significantly fewer action potentials were detected during the course of the touch
200 stimulus protocol in *Egfl6* knockout skin (Figure 3G). These results indicate that EGFL6
201 plays an important role in the excitation of Aδ-LTMRs.
202
203 **The bulge provides stable epidermal–neuronal interfaces**
204 Unlike most other sensory systems, the HF undergoes dynamic structural changes during
205 its periodic regeneration cycle (Figure 3–figure supplement 1E). It has remained unclear
206 how HFs are able to maintain stable HF–LC interactions over the course of this cycle. To
207 gain insight into this question, we first examined the changes that occur in the anatomical
208 structure of the upper-bulge epidermis during the hair regeneration cycle. We found that at
209 the first telogen (P20), the upper-bulge exhibits a single circular peripheral morphology
210 with one hair shaft, while at the first anagen (P35), the upper-bulge perimeter doubles due
211 to the formation of a new HF rostral to the existing HF (old bulge) (Figure 4A–C). At the
212 second telogen (P49), the upper-bulge perimeter decreased due to a reduction in the new
213 bulge perimeter. Thus, the external configuration of the rostral side of the upper-bulge
214 epidermis changes dynamically during the HF regeneration cycle, while the caudal aspect
215 remains stable.
216 We next examined the relationship between the dynamics of HF epidermal
217 morphology and LC structure. We measured the signal intensities of immuno-stained LC
218 components along the upper-bulge, and assigned average signal intensities to the position
219 angle of HFs. At the first telogen, HFs exhibited relatively regular signal intensities along

bioRxiv preprint doi: https://doi.org/10.1101/353490; this version posted June 22, 2018. The copyright holder for this preprint (which was not certified by peer review) is the author/funder, who has granted bioRxiv a license to display the preprint in perpetuity. It is made available under aCC-BY 4.0 International license.

220 the epidermal perimeter, but at the first anagen the new bulge (rostral side) showed areas of
221 low signal intensity, while these remained unchanged at the old (caudal) bulge (Figure 4A
222 and D). The low-intensity areas at new bulges became narrower in the second telogen. Both
223 Aδ- and C-LTMRs exhibited caudally polarized distribution in the second telogen (Figure
224 4–figure supplement 1A). Consistent with these signal intensity data, EGFL6 and tSCs in
225 the old bulge maintained regular parallel morphologies throughout the hair cycle, while
226 those in the new bulge exhibited diverse morphologies and wider widths in the first anagen
227 (Figure 4E, Figure 4–figure supplement 1B). Thus, the polarized distributions of LC
228 components toward the caudal side of the HFs are induced as the new bulge structure forms
229 at the rostral side of the HF. The caudal side of the HF, where the old bulge is maintained
230 by quiescent EpSCs, does not change in morphology, suggesting that the old bulge stably
231 preserves LCs irrespective of the stage of hair regeneration cycle.

232 Finally, we plucked a club hair, a retained hair from the previous hair cycle in the old
233 bulge, to test whether the removal of the sensor probe and subsequent alteration of the old
234 bulge architecture would affect the LC structure. The hairs were painted at the first telogen
235 (P20) and the painted hairs (i.e., club hairs) were plucked when the new hair and bulge
236 formed (Figure 4–figure supplement 1C). Three days after plucking, the old bulges
237 regressed (Figures 4F, Figure 4–figure supplement 1D), the LCs disappeared from the
238 caudal side of the upper-bulge, and ectopic LCs appeared at the rostral side of the upper-
239 bulge (Figure 4F and G). Together these results indicate that the preservation of the old
240 bulge epidermal structure provides a stable epidermal–neuronal interface and induces an
241 LC structure oriented toward the caudal side of the HF. Rutlin et al. (2014) reported that
242 caudally polarized localization of Aδ-LTMRs underlies direction-selective responsiveness
243 of Aδ-LTMRs to hair deflection, suggesting that the unique tissue architecture generated by
244 upper-bulge EpSCs is involved in the directional selectivity of the LCs.

bioRxiv preprint doi: https://doi.org/10.1101/353490; this version posted June 22, 2018. The copyright holder for this preprint (which was not certified by peer review) is the author/funder, who has granted bioRxiv a license to display the preprint in perpetuity. It is made available under aCC-BY 4.0 International license.

245

bioRxiv preprint doi: https://doi.org/10.1101/353490; this version posted June 22, 2018. The copyright holder for this preprint (which was not certified by peer review) is the author/funder, who has granted bioRxiv a license to display the preprint in perpetuity. It is made available under aCC-BY 4.0 International license.

Discussion

Our findings reveal transcriptional and anatomical roles of compartmentalized EpSCs in HF sensory unit formation (Figure 4H). Our previous study also showed that the mid-bulge EpSCs express many tendon-related genes and induce the differentiation of APMs and their correct anchorage to the bulge via secretion of the basement membrane protein nephronectin (Fujiwara et al., 2011). Deletion of nephronectin moves the muscle near the upper-bulge. The morphology of the LC was altered in the nephronectin mutant (Figure 4–figure supplement 1E–G), likely due to the changes in mechanical or geometrical environments of the upper-bulge by the mis-location of APMs. Therefore, we propose that the heterogeneous EpSCs are compartmentalized not only for efficient epidermal homeostasis and regeneration (Schepeler, Page, & Jensen, 2014), but also for defining patterned niches for specific epidermal–dermal interactions, in part through providing different ECM environments.

The biological significance of forming two bulges has not been well explained. A recent report by Lay, Kume, and Fuchs (2016) suggests that the two-bulge structure has an advantage for life-long HF epidermal maintenance as it increases the number of EpSCs and maintains SC quiescence by holding a keratin 6^+ inner bulge that expresses factors that inhibit SC activation. Our study now brings an entirely different perspective on the significance of the old bulge formation. We demonstrated that the formation and preservation of the old bulge provides a stable epidermal-neuronal interface and induces a LC structure oriented toward the caudal side of the hair follicle. Caudally polarized expression of BDNF in the bulge epidermis of developing HFs regulates caudally enriched localization of Aδ-LTMRs, which underlies direction-selective responsiveness of Aδ-LTMRs (Rutlin et al., 2014). Our data show that both Aδ-LTMRs and C-LTMRs become caudally polarized after the formation of the two-bulge structure, indicating that the unique

bioRxiv preprint doi: https://doi.org/10.1101/353490; this version posted June 22, 2018. The copyright holder for this preprint (which was not certified by peer review) is the author/funder, who has granted bioRxiv a license to display the preprint in perpetuity. It is made available under aCC-BY 4.0 International license.

tissue architecture provided by EpSCs is another major determinant of the formation, preservation and function of LCs in the HF.

The mechanisms to form and preserve proper innervation in regenerating HF have attracted attention. Botchkarev, Eichmuller, Johansson, and Paus (1997) reported the constant number of longitudinal nerve endings in the LCs in both natural and hair plucking-induced hair cycle. This invariance of nerve ending number, together with the unique epidermal tissue geometry and dynamics revealed in the present study, may underlie stability and topological reorganization of LCs during the hair cycle and in hair plucking-induced old bulge depletion.

We identified a novel electron-dense and amorphous ECM structure, which we named the collar matrix, that ensheathes LCs. The deletion of a collar matrix protein, EGFL6, impaired the structure and sensory function of LCs. The collar matrix has anatomical and functional features in common with the essential ECM in touch end organs of non-vertebrate organisms, such as the mantle in *C. elegans* (Emtage, Gu, Hartwieg, & Chalfie, 2004). Thus, electron-dense amorphous ECMs are likely to be the fundamental ECM regulating sensory end organ formation and function in multicellular organisms.

In conclusion, our findings give a new perspective on the roles played by heterogeneous and compartmentalized EpSC populations in more global aspects of organogenesis, beyond their role in epithelial maintenance and regeneration. Our study also provides insights into how sensory organs take advantage of a stable niche provided by a quiescent EpSC compartment to maintain sensory function within a structurally dynamic tissue environment.

bioRxiv preprint doi: https://doi.org/10.1101/353490; this version posted June 22, 2018. The copyright holder for this preprint (which was not certified by peer review) is the author/funder, who has granted bioRxiv a license to display the preprint in perpetuity. It is made available under aCC-BY 4.0 International license.

Author Contributions

C-C.C., K.T. and T.T. contributed equally to the study. C-C.C. and H.F. designed this study. C-C.C., N.S. A.N. and H.F. performed the mouse experiments. H.F., N.S., H.K. and Y.F. generated the *Egfl6-H2b-eGFP* mice. K.T. established the FACS protocols and purified the SC pools. K.T, C.T. and S.D.K. performed the RNA-seq and bioinformatics analysis. T.T. performed the electrophysiological analysis. C-C.C., K.K. and S.Y. performed the electron microscopic analysis. Y.T. provided COL4A3 and COL4A4 antibodies. F.M.W. oversaw the initial stage of this study. C-C.C., K.T., T.T. and H.F. wrote the paper with input from all authors.

Acknowledgments

We thank Shigehiro Kuraku, Yuichiro Hara, Osamu Nishimura of the RIKEN Phyloinformatics Unit for help in RNA-seq and bioinformatics; Hideki Enomoto for Ret-GFP mice; RIKEN Kobe light microscopy and animal facilities for technical assistance; Shigeo Hayashi and Douglas Sipp for their critical reading of the manuscript. We also thank the members of the Fujiwara laboratory for valuable reagents and discussion. This work was funded by RIKEN intramural funding, JSPS KAKENHI (25122720), Uehara Memorial Foundation, Takeda Science Foundation and Cosmetology Research Foundation (all to H.F.). C-C.C. was a recipient of the RIKEN-NSC Taiwan Fellowship. F.M.W. acknowledges financial support from the Medical Research Council, BBSRC and Wellcome Trust.

Competing Interests

The authors declare that no competing interests exist.

bioRxiv preprint doi: https://doi.org/10.1101/353490; this version posted June 22, 2018. The copyright holder for this preprint (which was not certified by peer review) is the author/funder, who has granted bioRxiv a license to display the preprint in perpetuity. It is made available under aCC-BY 4.0 International license.

319 **References:**

320 Bai, L., Lehnert, B. P., Liu, J., Neubarth, N. L., Dickendesher, T. L., Nwe, P. H., . . . Ginty,
321 D. D. (2015). Genetic Identification of an Expansive Mechanoreceptor Sensitive to
322 Skin Stroking. *Cell, 163*(7), 1783-1795. doi:10.1016/j.cell.2015.11.060

323 Botchkarev, V. A., Eichmuller, S., Johansson, O., & Paus, R. (1997). Hair cycle-dependent
324 plasticity of skin and hair follicle innervation in normal murine skin. *J Comp Neurol,*
325 *386*(3), 379-395.

326 Brownell, I., Guevara, E., Bai, C. B., Loomis, C. A., & Joyner, A. L. (2011). Nerve-derived
327 sonic hedgehog defines a niche for hair follicle stem cells capable of becoming
328 epidermal stem cells. *Cell Stem Cell, 8*(5), 552-565. doi:10.1016/j.stem.2011.02.021

329 Donati, G., & Watt, F. M. (2015). Stem cell heterogeneity and plasticity in epithelia. *Cell*
330 *Stem Cell, 16*(5), 465-476. doi:10.1016/j.stem.2015.04.014

331 Driskell, R. R., Giangreco, A., Jensen, K. B., Mulder, K. W., & Watt, F. M. (2009). Sox2-
332 positive dermal papilla cells specify hair follicle type in mammalian epidermis.
333 *Development, 136*(16), 2815-2823. doi:10.1242/dev.038620

334 Emtage, L., Gu, G., Hartwieg, E., & Chalfie, M. (2004). Extracellular proteins organize the
335 mechanosensory channel complex in C. elegans touch receptor neurons. *Neuron,*
336 *44*(5), 795-807. doi:10.1016/j.neuron.2004.11.010

337 Fujiwara, H., Ferreira, M., Donati, G., Marciano, D. K., Linton, J. M., Sato, Y., . . . Watt, F.
338 M. (2011). The basement membrane of hair follicle stem cells is a muscle cell niche.
339 *Cell, 144*(4), 577-589. doi:10.1016/j.cell.2011.01.014

340 Goodell, M. A., Nguyen, H., & Shroyer, N. (2015). Somatic stem cell heterogeneity:
341 diversity in the blood, skin and intestinal stem cell compartments. *Nat Rev Mol Cell*
342 *Biol, 16*(5), 299-309. doi:10.1038/nrm3980

bioRxiv preprint doi: https://doi.org/10.1101/353490; this version posted June 22, 2018. The copyright holder for this preprint (which was not certified by peer review) is the author/funder, who has granted bioRxiv a license to display the preprint in perpetuity. It is made available under aCC-BY 4.0 International license.

343 Jain, S., Golden, J. P., Wozniak, D., Pehek, E., Johnson, E. M., Jr., & Milbrandt, J. (2006).
344 RET is dispensable for maintenance of midbrain dopaminergic neurons in adult mice.
345 *J Neurosci, 26*(43), 11230-11238. doi:10.1523/JNEUROSCI.1876-06.2006
346 Jensen, U. B., Yan, X., Triel, C., Woo, S. H., Christensen, R., & Owens, D. M. (2008). A
347 distinct population of clonogenic and multipotent murine follicular keratinocytes
348 residing in the upper isthmus. *J Cell Sci, 121*(Pt 5), 609-617. doi:10.1242/jcs.025502
349 Koltzenburg, M., Stucky, C. L., & Lewin, G. R. (1997). Receptive properties of mouse
350 sensory neurons innervating hairy skin. *J Neurophysiol, 78*(4), 1841-1850.
351 Lay, K., Kume, T., & Fuchs, E. (2016). FOXC1 maintains the hair follicle stem cell niche
352 and governs stem cell quiescence to preserve long-term tissue-regenerating potential.
353 *Proc Natl Acad Sci U S A, 113*(11), E1506-1515. doi:10.1073/pnas.1601569113
354 Li, L., & Ginty, D. D. (2014). The structure and organization of lanceolate mechanosensory
355 complexes at mouse hair follicles. *Elife, 3*, e01901. doi:10.7554/eLife.01901
356 Li, L., Rutlin, M., Abraira, V. E., Cassidy, C., Kus, L., Gong, S., . . . Ginty, D. D. (2011).
357 The functional organization of cutaneous low-threshold mechanosensory neurons.
358 *Cell, 147*(7), 1615-1627. doi:10.1016/j.cell.2011.11.027
359 Lumpkin, E. A., Marshall, K. L., & Nelson, A. M. (2010). The cell biology of touch. *J Cell*
360 *Biol, 191*(2), 237-248. doi:10.1083/jcb.201006074
361 Mochizuki, T., Lemmink, H. H., Mariyama, M., Antignac, C., Gubler, M. C., Pirson, Y., . . .
362 et al. (1994). Identification of mutations in the alpha 3(IV) and alpha 4(IV) collagen
363 genes in autosomal recessive Alport syndrome. *Nat Genet, 8*(1), 77-81.
364 doi:10.1038/ng0994-77
365 Mouw, J. K., Ou, G., & Weaver, V. M. (2014). Extracellular matrix assembly: a multiscale
366 deconstruction. *Nat Rev Mol Cell Biol, 15*(12), 771-785. doi:10.1038/nrm3902

bioRxiv preprint doi: https://doi.org/10.1101/353490; this version posted June 22, 2018. The copyright holder for this preprint (which was not certified by peer review) is the author/funder, who has granted bioRxiv a license to display the preprint in perpetuity. It is made available under aCC-BY 4.0 International license.

Osada, A., Kiyozumi, D., Tsutsui, K., Ono, Y., Weber, C. N., Sugimoto, N., . . . Sekiguchi, K. (2005). Expression of MAEG, a novel basement membrane protein, in mouse hair follicle morphogenesis. *Exp Cell Res, 303*(1), 148-159. doi:10.1016/j.yexcr.2004.04.053

Rutlin, M., Ho, C. Y., Abraira, V. E., Cassidy, C., Bai, L., Woodbury, C. J., & Ginty, D. D. (2014). The cellular and molecular basis of direction selectivity of Adelta-LTMRs. *Cell, 159*(7), 1640-1651. doi:10.1016/j.cell.2014.11.038

Schepeler, T., Page, M. E., & Jensen, K. B. (2014). Heterogeneity and plasticity of epidermal stem cells. *Development, 141*(13), 2559-2567. doi:10.1242/dev.104588

Solanas, G., & Benitah, S. A. (2013). Regenerating the skin: a task for the heterogeneous stem cell pool and surrounding niche. *Nat Rev Mol Cell Biol, 14*(11), 737-748. doi:10.1038/nrm3675

Warming, S., Costantino, N., Court, D. L., Jenkins, N. A., & Copeland, N. G. (2005). Simple and highly efficient BAC recombineering using galK selection. *Nucleic Acids Res, 33*(4), e36. doi:10.1093/nar/gni035

Xiao, Y., Woo, W. M., Nagao, K., Li, W., Terunuma, A., Mukouyama, Y. S., . . . Brownell, I. (2013). Perivascular hair follicle stem cells associate with a venule annulus. *J Invest Dermatol, 133*(10), 2324-2331. doi:10.1038/jid.2013.167

Xin, T., Greco, V., & Myung, P. (2016). Hardwiring Stem Cell Communication through Tissue Structure. *Cell, 164*(6), 1212-1225. doi:10.1016/j.cell.2016.02.041

Zimmerman, A., Bai, L., & Ginty, D. D. (2014). The gentle touch receptors of mammalian skin. *Science, 346*(6212), 950-954. doi:10.1126/science.1254229

Zimmermann, K., Hein, A., Hager, U., Kaczmarek, J. S., Turnquist, B. P., Clapham, D. E., & Reeh, P. W. (2009). Phenotyping sensory nerve endings in vitro in the mouse. *Nat Protoc, 4*(2), 174-196. doi:10.1038/nprot.2008.223

bioRxiv preprint doi: https://doi.org/10.1101/353490; this version posted June 22, 2018. The copyright holder for this preprint (which was not certified by peer review) is the author/funder, who has granted bioRxiv a license to display the preprint in perpetuity. It is made available under aCC-BY 4.0 International license.

392

bioRxiv preprint doi: https://doi.org/10.1101/353490; this version posted June 22, 2018. The copyright holder for this preprint (which was not certified by peer review) is the author/funder, who has granted bioRxiv a license to display the preprint in perpetuity. It is made available under aCC-BY 4.0 International license.

Figures

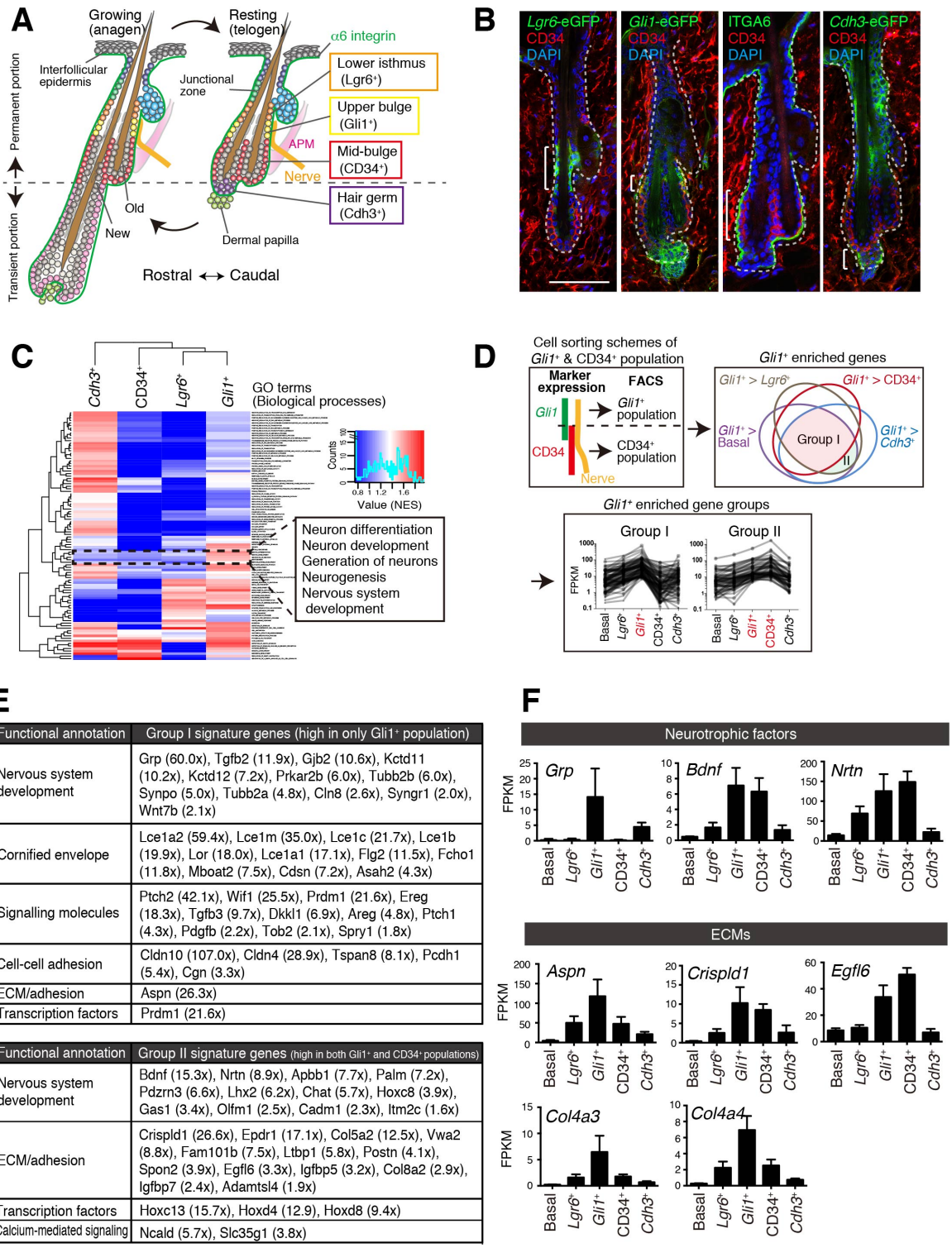

E

Functional annotation	Group I signature genes (high in only Gli1+ population)
Nervous system development	Grp (60.0x), Tgfb2 (11.9x), Gjb2 (10.6x), Kctd11 (10.2x), Kctd12 (7.2x), Prkar2b (6.0x), Tubb2b (6.0x), Synpo (5.0x), Tubb2a (4.8x), Cln8 (2.6x), Syngr1 (2.0x), Wnt7b (2.1x)
Cornified envelope	Lce1a2 (59.4x), Lce1m (35.0x), Lce1c (21.7x), Lce1b (19.9x), Lor (18.0x), Lce1a1 (17.1x), Flg2 (11.5x), Fcho1 (11.8x), Mboat2 (7.5x), Cdsn (7.2x), Asah2 (4.3x)
Signalling molecules	Ptch2 (42.1x), Wif1 (25.5x), Prdm1 (21.6x), Ereg (18.3x), Tgfb3 (9.7x), Dkkl1 (6.9x), Areg (4.8x), Ptch1 (4.3x), Pdgfb (2.2x), Tob2 (2.1x), Spry1 (1.8x)
Cell-cell adhesion	Cldn10 (107.0x), Cldn4 (28.9x), Tspan8 (8.1x), Pcdh1 (5.4x), Cgn (3.3x)
ECM/adhesion	Aspn (26.3x)
Transcription factors	Prdm1 (21.6x)

Functional annotation	Group II signature genes (high in both Gli1+ and CD34+ populations)
Nervous system development	Bdnf (15.3x), Nrtn (8.9x), Apbb1 (7.7x), Palm (7.2x), Pdzrn3 (6.6x), Lhx2 (6.2x), Chat (5.7x), Hoxc8 (3.9x), Gas1 (3.4x), Olfm1 (2.5x), Cadm1 (2.3x), Itm2c (1.6x)
ECM/adhesion	Crispld1 (26.6x), Epdr1 (17.1x), Col5a2 (12.5x), Vwa2 (8.8x), Fam101b (7.5x), Ltbp1 (5.8x), Postn (4.1x), Spon2 (3.9x), Egfl6 (3.3x), Igfbp5 (3.2x), Col8a2 (2.9x), Igfbp7 (2.4x), Adamtsl4 (1.9x)
Transcription factors	Hoxc13 (15.7x), Hoxd4 (12.9), Hoxd8 (9.4x)
Calcium-mediated signaling	Ncald (5.7x), Slc35g1 (3.8x)

F

Fig. 1 Cheng *et al.*

Figure 1. Upper-bulge EpSCs are molecularly specialized for HF–nerve interactions

(**A**) Graphical illustration of EpSC compartments. APM, arrector pili muscle. (**B**) Distinct

bioRxiv preprint doi: https://doi.org/10.1101/353490; this version posted June 22, 2018. The copyright holder for this preprint (which was not certified by peer review) is the author/funder, who has granted bioRxiv a license to display the preprint in perpetuity. It is made available under aCC-BY 4.0 International license.

397 EpSC compartments in 8-week-old telogen skin were visualized with specific eGFP
398 reporters and cell surface markers. Brackets indicate target cell populations for sorting. (**C**)
399 Z-score heat map representing the normalized enrichment score (NES) of GSEA using the
400 transcriptome data of each EpSC population. (**D**) Scheme of the extraction of genes highly
401 expressed in the *Gli1*$^+$ population (Group I) and in both the *Gli1*$^+$ and CD34$^+$ populations
402 (Group II). (**E**) Lists of the genes highly expressed in *Gli1*$^+$ population (Group I) and in both
403 *Gli1*$^+$ and CD34$^+$ populations (Group II). (**F**) Expression levels of neurotrophic factor and
404 ECM genes highly expressed in upper-bulge SCs. Basal, basal EpSC pool. Data are mean ±
405 SD, n = 3-4.
406

bioRxiv preprint doi: https://doi.org/10.1101/353490; this version posted June 22, 2018. The copyright holder for this preprint (which was not certified by peer review) is the author/funder, who has granted bioRxiv a license to display the preprint in perpetuity. It is made available under aCC-BY 4.0 International license.

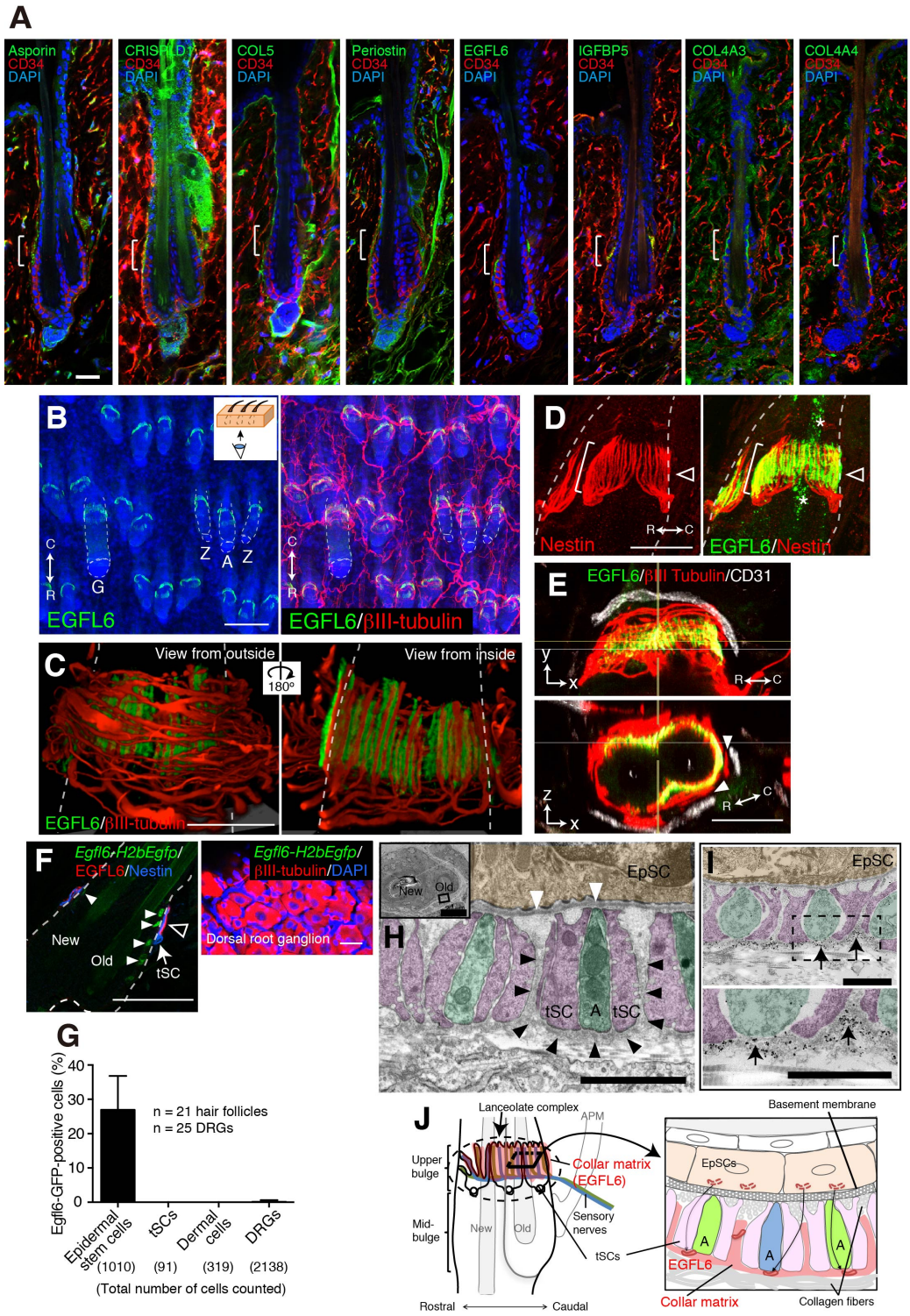

Fig. 2 Cheng *et al.*

407

408 **Figure 2. Upper-bulge EpSCs deposit EGFL6 into the collar matrix (A)**

409 Immunostaining pattern of upper-bulge-specific ECM in 8-week-old telogen skin. Brackets:

bioRxiv preprint doi: https://doi.org/10.1101/353490; this version posted June 22, 2018. The copyright holder for this preprint (which was not certified by peer review) is the author/funder, who has granted bioRxiv a license to display the preprint in perpetuity. It is made available under aCC-BY 4.0 International license.

410 upper-bulge. (**B**) EGFL6 was colocalized with βIII-tubulin$^+$ nerve endings in the upper-
411 bulge of dorsal guard ('G'), awl/auchene ('A') and zigzag ('Z') HFs. (**C**) Magnified images
412 of EGFL6 and βIII-tubulin in telogen skin. (**D**) The protrusions of the tSCs (white brackets)
413 were colocalized with EGFL6 in the upper-bulge of 8-week-old telogen HF (open
414 arrowheads). Asterisks: nonspecific signals. (**E**) CD31$^+$ blood vessels did not show direct
415 contact to EGFL6 in 7-week-old telogen HF. Arrowheads: gaps between EGFL6 (green)
416 and blood vessels (white). (**F**) The dorsal skin and dorsal root ganglia (DRG) of an 8-week-
417 old *Egfl6-H2b-Egfp* mouse was stained for eGFP, EGFL6, nestin and βIII-tubulin. eGFP
418 (closed arrowheads) staining was observed in the upper-bulge (open arrowhead) epidermis
419 of old bulge (Old), but not in other cellular components around the upper-bulge. (**G**)
420 Statistical examination of *Egfl6*-H2BeGFP-positive cells around the upper bulge. Data are
421 mean ± SD. (**H**) A transmission electron microscopic image of the upper-bulge of P35
422 zigzag HF. An electron-dense amorphous ECM structure, the collar matrix (black
423 arrowheads), ensheathed LC endings [A, axon (green); tSC (pink); EpSC (gold); white
424 arrowheads, epidermal basement membrane]. (**I**) The EGFL6-gold particles were localized
425 in the collar matrix (arrows). (**J**) Schematic representation of the localization of EGFL6 in
426 the upper-bulge. Scale bars, 10 μm (A), 20 μm (C-F), 100 μm (B), 2 μm (H), 1 μm (I).
427

bioRxiv preprint doi: https://doi.org/10.1101/353490; this version posted June 22, 2018. The copyright holder for this preprint (which was not certified by peer review) is the author/funder, who has granted bioRxiv a license to display the preprint in perpetuity. It is made available under aCC-BY 4.0 International license.

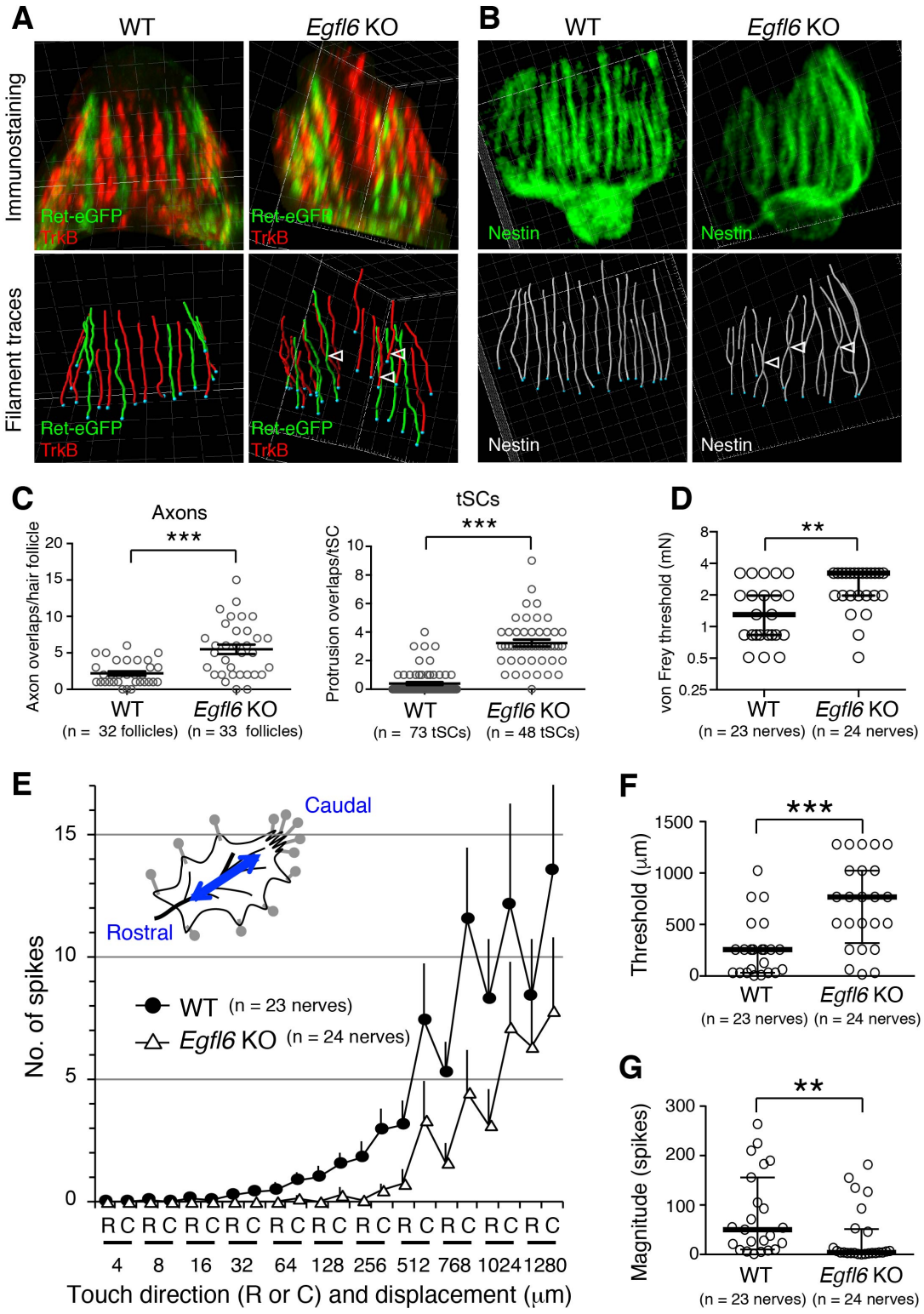

Fig. 3 Cheng *et al.*

Figure 3. EGFL6 is required for the patterning and touch responses of LCs (**A** and **B**) 3D reconstituted images and filament tracings of axonal endings (A) and tSCs (B) in the old bulge of wild-type and *Egfl6* knockout 8-week-old skin. *Ret*-eGFP, a marker for C-LTMRs

bioRxiv preprint doi: https://doi.org/10.1101/353490; this version posted June 22, 2018. The copyright holder for this preprint (which was not certified by peer review) is the author/funder, who has granted bioRxiv a license to display the preprint in perpetuity. It is made available under aCC-BY 4.0 International license.

and TrkB, a marker for Aδ-LTMRs. Open arrowhead: overlapping points of axonal endings and tSC processes. Grid width, 5 μm. (**C**) Overlapping points of axonal endings and tSC processes were counted. Data are mean ± SEM. Two-tailed unpaired *t*-test. (**D**) Mechanical sensitivity of Aδ-LTMRs was analyzed using von Frey hairs in wild-type and *Egfl6* knockout skin–nerve preparations from 10-12 week-old telogen skin. (**E**) Touch response patterns of Aδ-LTMRs in wild-type and *Egfl6* knockout skin–nerve preparations. A ramp-and-hold touch stimulus was applied using a piezo-controlled micromanipulator (see Methods and Figure 3–figure supplement 2A). (**F**) Threshold displacement of Aδ-LTMRs. (**G**) Number of action potentials during the course of the touch stimulus protocol (i.e., magnitude of touch responses) was measured. Data in (D, F, G) are median with interquartile range (IQR) and in (E) are mean ± SEM. Statistics: Mann-Whitney U-test (D, F, G).

bioRxiv preprint doi: https://doi.org/10.1101/353490; this version posted June 22, 2018. The copyright holder for this preprint (which was not certified by peer review) is the author/funder, who has granted bioRxiv a license to display the preprint in perpetuity. It is made available under aCC-BY 4.0 International license.

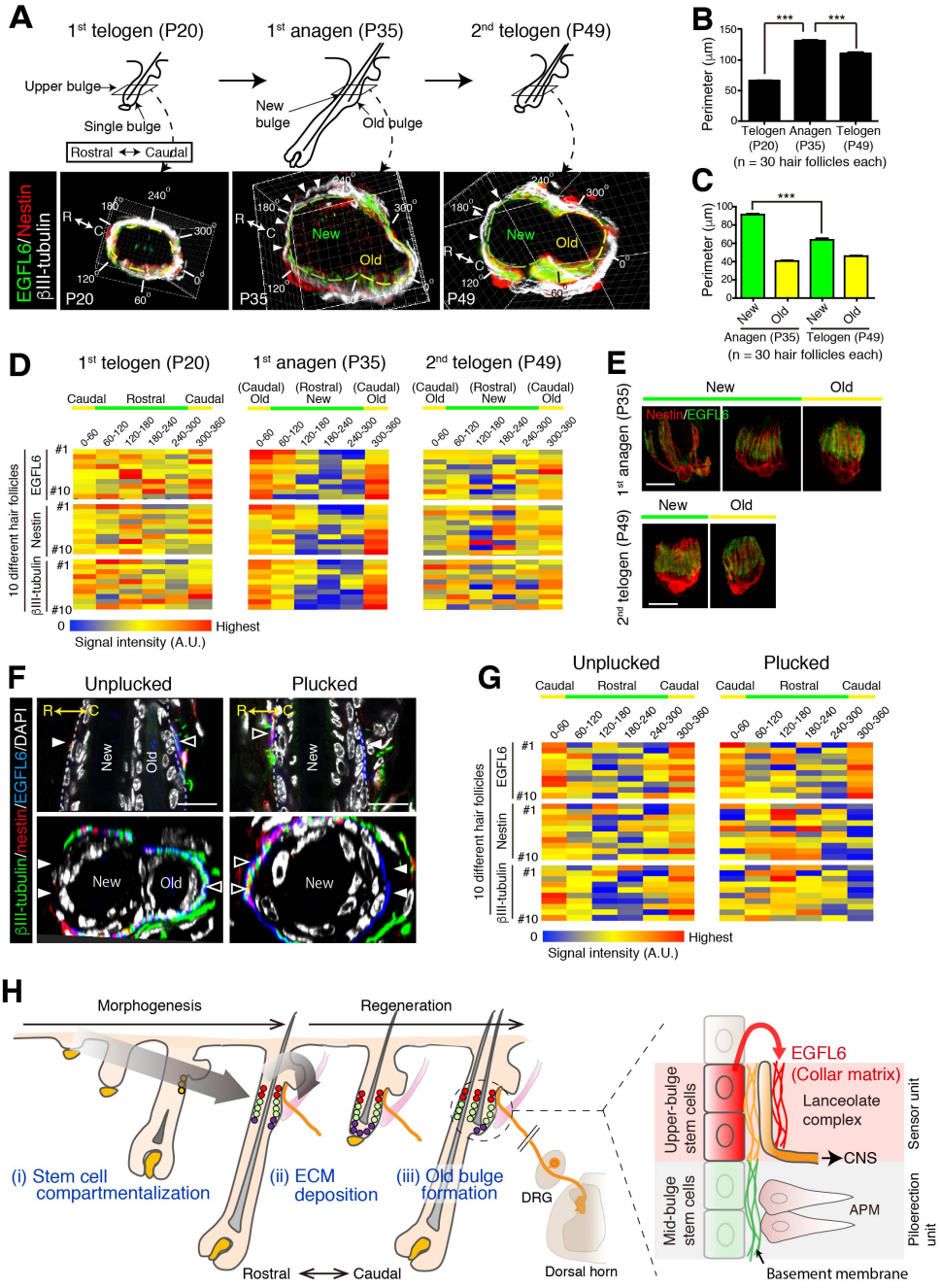

Fig. 4 Cheng *et al.*

Figure 4. The old bulge provides stable epidermal–neuronal interfaces (**A**) Structural changes of the upper-bulge during the HF regeneration cycle. Cross-sectional views of the upper-bulge of zigzag HFs are shown. Closed arrowheads indicate a large gap of LCs. (**B**) Perimeter length of the upper-bulge and (C) the upper-bulge of new and old bulges. (**D**) Heat map of the relative signal intensity levels of EGFL6, nestin and βIII-tubulin along the

bioRxiv preprint doi: https://doi.org/10.1101/353490; this version posted June 22, 2018. The copyright holder for this preprint (which was not certified by peer review) is the author/funder, who has granted bioRxiv a license to display the preprint in perpetuity. It is made available under aCC-BY 4.0 International license.

upper-bulge perimeter. Geometry of the upper-bulge perimeter is shown above the heat map. (**E**) Morphological differences of EGFL6/tSC complexes in new and old bulges. (**F**) Sagittal and transverse sectional views of the upper-bulge in P35 anagen HFs with the club hair unplucked and plucked. Open and closed arrowheads indicate areas with and without LCs, respectively. (**G**) Heat map of the relative signal intensity levels of EGFL6, nestin and βIII-tubulin along the upper-bulge perimeter in HFs with the club hair unplucked and plucked. (**H**) Schematic summary of the contribution of EpSCs to sensory unit formation. (i) During development, EpSCs for HF–nerve interactions are induced and compartmentalized in the upper-bulge. (ii) Upper-bulge EpSCs provide specialized ECM and neurogenetic environments for LCs. (iii) EpSCs maintain an old bulge at the caudal side of the HF, providing stable HF–nerve interfaces. Scale bars, 10 μm.

bioRxiv preprint doi: https://doi.org/10.1101/353490; this version posted June 22, 2018. The copyright holder for this preprint (which was not certified by peer review) is the author/funder, who has granted bioRxiv a license to display the preprint in perpetuity. It is made available under aCC-BY 4.0 International license.

Materials and methods

Mice

Egfl6 knockout mice (032277-UCD) were obtained from the Mutant Mouse Resource & Research Centers (MMRRC). Lack of *Egfl6* mRNA and EGFL6 protein were confirmed by *in situ* hybridization and immunostaining. *Egfl6-H2b-Egfp* BAC transgenic mice were generated as described below. *Ret-eGFP* knock-in mice have been described previously (Jain et al., 2006) and kindly provided by H. Enomoto (Kobe University). *Lgr6-GFP-ires-CreERT2* mice were obtained from Jackson Laboratory. *Gli1-eGFP* mice (STOCK Tg(Gli1-EGFP)DM197Gsat/Mmucd) and *Cdh3-eGFP* mice (STOCK Tg(Cdh3-EGFP)BK102Gsat/Mmnc) were obtained from MMRRC. Mouse lines used for transcriptome analysis were backcrossed with C57BL/6N mice more than 4 times. C57BL/6N and BALB/c mice were obtained from Japan SLC Inc. *Npnt* floxed mice were obtained from Jackson Laboratory and crossed with keratin 5-Cre mice from the Jose Jorcano laboratory. All animal experiments were conducted and performed in accordance with approved Institutional Animal Care and Use Committee protocols.

Generation of the *Egfl6-H2b-Egfp* mouse line

Egfl6-H2b-Egfp BAC transgenic mice (Accession No. CDB0518T: http://www2.clst.riken.jp/arg/TG%20mutant%20mice%20list.html) were generated by introducing a BAC carrying a *H2b-Egfp* transgene just before the ATG of the mouse *Egfl6* gene. The BAC clone RP23-124O13, containing the full genomic sequence of *Egfl6*, was obtained from CHORI BACPAC Resources Center. The *H2b-Egfp* fusion gene was introduced just before the first coding ATG of the *Egfl6* gene in the BAC clone using a two-step selection BAC recombineering protocol (Warming, Costantino, Court, Jenkins, & Copeland, 2005). The modified BAC construct was purified with a NucleoBond Xtra Midi

bioRxiv preprint doi: https://doi.org/10.1101/353490; this version posted June 22, 2018. The copyright holder for this preprint (which was not certified by peer review) is the author/funder, who has granted bioRxiv a license to display the preprint in perpetuity. It is made available under aCC-BY 4.0 International license.

kit (Macherey-Nagel) and injected into the pronuclei of fertilized one-cell mouse eggs derived from the breeding of BDF1 and C57BL/6N mice. Potential founder mice were screened by genomic PCR of ear biopsy DNA with following primers: 5'-CCAAGGTCCTGACCAGCGAAG-3' and 5'- CCTTAGTCACCGCCTTCTTGGAG -3' (product size: 163 base pairs). These primers were also used for routine genotyping of this mouse line. The transgene-positive founder mice were bred with wild-type C57BL/6N mice and some of the offspring were used for immunostaining of eGFP to confirm the expression and nuclear localization of the H2B-eGFP protein. We have established 16 nuclear-GFP-positive transgenic mouse lines and confirmed the GFP expression in the upper bulge in 13 mouse lines.

Cell lines

Cell lines used in this study were 293F cells (Thermo Fisher), human primary keratinocytes (Watt lab), human embryonic kidney epithelial cell line HEK293 (RIKEN Bioresource Center), human glioblastoma cell line T98G (JCRB Cell Bank), Human glioma cell line KG-1-C (JCRB Cell Bank), human skin fibroblast cell line SF-TY (JCRB Cell Bank), human embryonic fibroblast cell line NTI-4 (JCRB Cell Bank), human sarcoma cell line HT-1080 (JCRB Cell Bank), human myelogenous leukemia cell line K562 (JCRB Cell Bank) and human myelogenous leukemia cell line transfected with human integrin α8 cDNA K562-a8 (Gift from L. Reichardt).

Human primary keratinocytes were cultured on irradiated J2 feeder cells with DMEM/Ham's F12 medium supplemented with 10% FBS, 0.5 μg/ml hydrocortisone (Sigma), 0.1 nM cholera toxin (Sigma), 10 μg/ml EGF (Peprotech), 2 mM GlutaMax (Invitrogen) and 5 μg/ml Insulin (Sigma) at 37 °C under 5% CO_2. Other cell lines were cultured according to the cell culture instructions from each source cell bank or company.

bioRxiv preprint doi: https://doi.org/10.1101/353490; this version posted June 22, 2018. The copyright holder for this preprint (which was not certified by peer review) is the author/funder, who has granted bioRxiv a license to display the preprint in perpetuity. It is made available under aCC-BY 4.0 International license.

513

514 **Antibodies**

515 Antibodies used in this study were listed in Table 1.

516

517 **Generation of antibodies**

518 Rabbit antiserum to mouse EGFL6 was generated by immunizing rabbits with a Myc-His-
519 tagged Mucin-MAM domain of recombinant mouse EGFL6 (S257-G550). The antigen was
520 expressed in the 293F mammalian expression system (Invitrogen) and purified from the
521 supernatant of the transfected cells with a Ni-NTA column. The antibody in the antiserum
522 was affinity-purified with an antigen conjugated CNBr-activated Sepharose 4B. The
523 specificity of the antibody to mouse EGFL6 was confirmed by the absence of the antibody
524 immunoreactivity to tissue samples from *Egfl6* knockout mice. Rabbit antiserum to mouse
525 nephronectin was generated by the same method described above. Recombinant flag-tagged
526 full-length mouse nephronectin was expressed in 293F cells and purified with a FLAG-M2
527 immuno-affinity column (Sigma). The antibody in the antiserum was affinity-purified with
528 a CNBr-activated Sepharose 4B conjugated with purified His-tagged mouse full-length
529 nephronectin. The specificity of the antibody to mouse nephronectin was confirmed by the
530 absence of the antibody immunoreactivity to tissue samples from *Npnt* knockout mice.

531

532 **FACS**

533 Mouse adult dorsal telogen keratinocytes were isolated and stained for cell surface markers
534 as described previously (Fujiwara et al., 2011) with some modifications. We utilized *Lgr6-*
535 *GFP-ires-CreERT2*, *Gli1-eGFP* and *Cdh3-eGFP* mice to fluorescently visualize the
536 epidermal stem cells in the lower isthmus (*Lgr6*$^+$), upper bulge (*Gli1*$^+$), and hair germ
537 (*Cdh3*$^+$) with eGFP. Dissected dorsal skin of the 8-week-old female mice was treated with

bioRxiv preprint doi: https://doi.org/10.1101/353490; this version posted June 22, 2018. The copyright holder for this preprint (which was not certified by peer review) is the author/funder, who has granted bioRxiv a license to display the preprint in perpetuity. It is made available under aCC-BY 4.0 International license.

538 0.25% trypsin solution (Nakalai tesque) at 37°C for 1 hr. The epidermal tissue was scraped
539 off from the dermal tissue with a scalpel. This epidermis separation protocol leaves hair
540 germ cells in the dermal tissue. Effectiveness of this tissue separation was verified by the
541 following qRT-PCR, RNA-seq and immunohistochemical analyses with compartment-
542 specific markers as described below. For the sorting of lower isthmus (*Lgr6*-eGFP$^+$), upper-
543 bulge (*Gli1*-eGFP$^+$) and mid-bulge (CD34$^+$) epidermal stem cells, the separated epidermis
544 was minced with scalpels and mixed with repeated pipetting to make a single cell suspension.
545 To deplete haematopoietic and endothelial cells (lineage-positive cells; Lin$^+$), the cell
546 suspension was stained with PE-Cy7-conjugated antibodies for CD45, TER-119 and CD31.
547 To sort the target cells, the cell suspension was also stained with Sca-1-PerCP-Cy5.5, CD34-
548 eFluor660, CD49f (integrin α6)-PE. Sca-1 was used to remove epidermal basal cells of the
549 interfollucular epidermis and follicle infundibulum (Jensen et al., 2008). Cells were sorted
550 with a FACSAria II according to the expression of cell surface markers, after gating out
551 dead and Lin$^+$ cells (Figure 1–figure supplement 1A).

552 Hair germ epidermal cells (*Cdh3*-eGFP$^+$) were sorted from the remaining dermal
553 tissue since the most hair germ epidermal cells were retained in the dermal tissue after the
554 separation of the epidermis. The dermal tissue was minced with scalpels and incubated with
555 2 mg/ml of collagenase type I at 37°C for 2 hr with gentle mixing. Single cell suspension
556 was obtained by repeated pipetting. The cell suspension was stained with the same
557 antibodies used above and subjected to the sorting procedure.

558 The purity of sorted cells was confirmed by qRT-PCR with compartment-specific
559 genes: *Lrig1* (junctional zone and lower-isthmus), *Lgr6* (lower-isthmus and upper bulge),
560 *Gli1* (upper-bulge and hair germ), *Bdnf* (upper-bulge), *Cd34* (mid-bulge), *Cdh3* (hair germ)
561 (Figure 1–figure supplement 1B). While the expression of *Gli1*-eGFP was detected in both
562 upper-bulge and hair germ regions (Figure 1B), our cell isolation and sorting methods gave

bioRxiv preprint doi: https://doi.org/10.1101/353490; this version posted June 22, 2018. The copyright holder for this preprint (which was not certified by peer review) is the author/funder, who has granted bioRxiv a license to display the preprint in perpetuity. It is made available under aCC-BY 4.0 International license.

563 highly pure upper-bulge cells and hair germ cells, respectively. For example, a marker for
564 upper-bulge cells, *Bdnf*, was highly enriched in *Gli1*+ upper bulge cells, but not in *Cdh3*+
565 hair germ cells (Figure 1–figure supplement 1B). On the other hand, the expression of *Cdh3*,
566 a marker for hair germ cells, was high in the *Cdh3*+ hair germ population, but was very low
567 in the *Gli1*+ upper-bulge population (Figure 1–figure supplement 1B). We identified *Spon1*
568 as a gene exclusively expressed in the hair germ from our gene expression profiling of
569 isolated stem cell populations and confirmed that it was not detected in the *Gli1*+ upper-
570 bulge population (Figure 1–figure supplement 1C). Subsequent protein tissue-localization
571 analysis of compartment-specific genes, which were identified in our gene expression
572 profiling, further confirmed the validity and purity of sorted cells. For example, gene
573 products of upper-bulge-enriched ECM genes, including *Aspn*, *Crispld1*, *Egfl6*, *Col4a3* and
574 *Col4a4,* were deposited in the upper-bulge (Figure 2A), while SPON1 protein was localized
575 in the hair germ region, but not in the upper-bulge. Collectively, our data demonstrate that
576 the purity of each isolated stem cell population was very high.
577
578 **qRT-PCR**
579 Total RNA was extracted from the sorted cells using an RNeasy micro kit (Qiagen). qRT-
580 PCR was performed to determine target cell populations using Power SYBR Green PCR
581 Master Mix (Life Technologies) with specific primer sets (Table 2) on 7900HT real-time
582 PCR system (Applied Biosystems).
583
584 **RNA library preparation and sequencing**
585 For each library, isolated total RNA samples were quantified with the Qubit RNA HS Assay
586 Kit on a Qubit Fluorometer (Thermo Fisher Scientific), and their qualities were analyzed
587 with the RNA 6000 Pico Kit on a 2100 Bioanalyzer (Agilent Technologies). Qubit

bioRxiv preprint doi: https://doi.org/10.1101/353490; this version posted June 22, 2018. The copyright holder for this preprint (which was not certified by peer review) is the author/funder, who has granted bioRxiv a license to display the preprint in perpetuity. It is made available under aCC-BY 4.0 International license.

588 measurements were used to ensure that each library was prepared with 10 ng of total RNA.
589 Library preparation was processed following the TruSeq Stranded mRNA Sample Prep Kit
590 (Illumina) protocol till adapter ligation, except that the duration of the initial RNA
591 fragmentation was shortened to 7 minutes. The adapter-ligated cDNA was amplified with
592 14 PCR cycles. The prepared libraries were sequenced using the Rapid Run mode with 80
593 cycles on the HiSeq1500 (Illumina), operated by HiSeq Control Software v2.2.58 using
594 HiSeq SR Rapid Cluster Kit v2 (Illumina) and HiSeq Rapid SBS Kit v2 (Illumina). Base
595 calling was performed with RTA v1.18.64 and the fastq files were generated with bcl2fastq
596 v1.8.4 (Illumina).
597
598 **Mapping and expression quantification**
599 Qualities of the RNA-seq reads were evaluated with FastQC v0.11.3. The program
600 fastq_quality_filter, part of the FASTX Toolkit v0.0.14, was used to trim bases with a
601 quality value below 30. Additionally, if more than 20% of the bases of a read were removed
602 by this trimming procedure, then the whole read was discarded. Once this quality trim was
603 completed, Trim_galore v0.3.3 was executed to remove adapter sequences from the 3'-ends
604 of reads, and to discard reads that were shorter than 50nt. The processed reads were mapped
605 to the mm10 mouse genome assembly, obtained from iGenomes
606 (http://support.illumina.com/sequencing/sequencing_software/igenome.html), using the
607 splice-aware aligner TopHat v2.0.14 with default parameter settings. Reads mapping to
608 ribosomal DNA accounted for ~1% of the total number of reads in each library, and were
609 removed. Details for each library concerning sequencing and read statistics, including the
610 total amount that uniquely mapped to the genome, are displayed in Table 3.
611 Gene expression quantification was performed using the Cuffdiff program in the
612 Cufflinks package v2.2.1, with the frag-bias-correction and multi-read-correction options

bioRxiv preprint doi: https://doi.org/10.1101/353490; this version posted June 22, 2018. The copyright holder for this preprint (which was not certified by peer review) is the author/funder, who has granted bioRxiv a license to display the preprint in perpetuity. It is made available under aCC-BY 4.0 International license.

613 enabled. Cuffdiff used the mm10 gene model obtained from iGenomes to estimate the
614 number of fragments that originated from individual genes. For each gene, in addition to
615 this produced raw count data, Cuffdiff also calculated normalized expression values, which
616 are referred to as fragments per kilobase of transcript per million mapped reads (FPKM).
617
618 **GO and clustering analysis**
619 FPKM values from RNA-seq data were analysed by Gene Ontology (GO) term enrichment
620 analysis. Genes with low expression (FPKM < 5) were filtered out and considered not
621 expressed. Then the remaining FPKM values were log2-transformed for further analysis.
622 To characterize global gene expression profiles of each epidermal stem cell population, gene
623 set enrichment analysis (GSEA) was performed using GSEA software (2.2.2 from Broad
624 Institute) with GO biological processes as a gene set collection (c5.bp.v5.1.symbols.gmt).
625 In this analysis, pairwise differences between basal epidermal stem cells and each epidermal
626 stem cell population were examined. The normalized enrichment score (NES) and False
627 Discovery Rate (FDR) were calculated for each gene set and compared among cell
628 populations using a bioconductor R with heatmap.2 gplots package.
629
630 **Immunohistochemistry and imaging**
631 Whole-mount immunostaining and horizontal imaging of mouse dorsal skin were
632 performed as described previously (Fujiwara et al., 2011). Vertical whole-mount imaging
633 of dorsal and whisker skin was performed as described below. Mouse skin tissues were
634 dissected and fixed with 4% paraformaldehyde/PBS for 1 hr at 4^{o}C. Fixed tissues were
635 washed and embedded in OCT compound and frozen on liquid nitrogen. Vertical skin
636 sections (150 μm thick) were made using a cryostat (Leica) and washed with PBS to remove
637 remnant OCT compound. Skin sections were blocked with a blocking buffer (0.5% skim

bioRxiv preprint doi: https://doi.org/10.1101/353490; this version posted June 22, 2018. The copyright holder for this preprint (which was not certified by peer review) is the author/funder, who has granted bioRxiv a license to display the preprint in perpetuity. It is made available under aCC-BY 4.0 International license.

638 milk/0.25% fish skin gelatin/0.5% Triton X-100/PBS) for 1 hr at 4°C and then incubated
639 with primary antibodies diluted in blocking buffer overnight at 4°C. Skin samples were
640 washed with 0.2% Tween 20/PBS for 4 hr and then incubated with DAPI and secondary
641 antibodies diluted in blocking buffer overnight at 4°C. Finally, skin samples were washed
642 with 0.2% Tween20/PBS for 4 hr at 4°C and mounted with BABB clearing solution. Images
643 were acquired using a Leica TSC SP8. Z stack maximum projection images and three
644 dimensional reconstructed images of skin whole-mount preparation were produced using
645 Imaris 4D rendering software (Bitplane) and Volocity 3D imaging software (Perkin Elmer).
646

647 **Transmission electron microscopy**

648 Dissected skin tissues were immediately immersed in 2% fresh formaldehyde and 2.5%
649 glutaraldehyde in 0.1M sodium cacodylate buffer (pH 7.4), sliced into 0.5-1 mm-thin
650 sections with a scalpel and fixed for 2 hr at room temperature. After washing three times
651 with 0.1M cacodylate buffer (pH 7.4) for 5 min, tissues were post-fixed with ice-cold 1%
652 OsO_4 in the same buffer for 2 hr. Samples were rinsed with distilled water, stained with
653 0.5% aqueous uranyl acetate for 2 hr or overnight at room temperature, then dehydrated
654 with ethanol and propylene oxide, and embedded in Poly/Bed 812 (Polyscience). Ultra-thin
655 sections were cut, doubly-stained with uranyl acetate and Reynold's lead citrate, and viewed
656 with a JEM 1010 or JEM 1400 plus transmission electron microscope (JEOL) at an
657 accelerating voltage of 100 kV.
658

659 **Immunoelectron microscopy**

660 Skin samples were dissected, fixed and stained according to the whole-mount
661 immunostaining method. In-house rabbit EGFL6 antibody was used as the primary antibody
662 and Alexa Fluor 488 FluoroNanogold-anti rabbit IgG (Nanoprobes) (1:200 dilution) was

bioRxiv preprint doi: https://doi.org/10.1101/353490; this version posted June 22, 2018. The copyright holder for this preprint (which was not certified by peer review) is the author/funder, who has granted bioRxiv a license to display the preprint in perpetuity. It is made available under aCC-BY 4.0 International license.

used for the secondary antibody. After confirming the localization of Alexa Fluor 488 labelled EGFL6 under a fluorescent microscope, the samples were fixed for 1 hr in 1% glutaraldehyde in PBS. GoldEnhance EM (Nanoprobes) was used in accordance with the manufacturer's protocol to enlarge the size of gold particles. Samples were then embedded in resin (poly/bed 812; Polyscience). Ultrathin sections were stained with uranyl acetate and lead citrate before observation with an electron microscope (JEM 1400 plus; JEOL).

Quantification of axon and tSC processes

Neural filaments and tSC protrusions were visualized, measured and analysed using the Imaris software program FilamentTracer (Bitplane). To detect Aδ- and C-LTMRs and tSCs in *Egfl6* knockout mice, we crossed *Egfl6* knockout mice with *Ret-eGFP* knock-in mice (Jain et al., 2006) that express eGFP in C-LTMRs (Li et al., 2011). Skin whole-mounts were immunostained for TrkB, eGFP and nestin to visualize Aδ- and C-LTMRs and tSCs, respectively. To examine the structure of lanceolate complexes, we analysed old bulge regions, but not new bulge regions, since the new bulge regions tend to show a small amount of EGFL6 and an irregular shape of lanceolate complexes. Axon endings and tSC processes were automatically detected in three dimensionally reconstructed immunohistochemical images using FilamentTracer. Traced axonal endings and tSC protrusions were visualized as fixed-diameter cylinders in green (*Ret*-eGFP), red (TrkB) and white (nestin). Length, number and width of axon endings and tSC processes were automatically measured by the software. Overlapped filament points were detected three-dimensionally using the cylinder display mode.

For the measurement of the upper-bulge perimeter, immunostained whole-mount z-stack images were reconstituted to 3D images with Imaris 7.2.1 software. An Imaris Oblique Slicer function was used to make a plane cutting through the region of tSC processes and

bioRxiv preprint doi: https://doi.org/10.1101/353490; this version posted June 22, 2018. The copyright holder for this preprint (which was not certified by peer review) is the author/funder, who has granted bioRxiv a license to display the preprint in perpetuity. It is made available under aCC-BY 4.0 International license.

688 this plane was defined as a measurement layer. The perimeter of the hair follicle was traced
689 and the length of the trace was automatically measured by the software.
690
691 **Quantification of the expressions of *Egfl6*-H2BeGFP and αv integrins**
692 GFP expression in *Egfl6*-H2BeGFP reporter mice were used to examine the expression of
693 *Egfl6* transcripts. Adult telogen dorsal skin of *Egfl6*-H2BeGFP mice were immunostained
694 for GFP, keratin 14 (marker for basal keratinocytes) and nestin (marker for tSCs), with
695 DAPI nuclear counter staining, as described above. Vertical 3D images of zigzag hair
696 follicles were obtained. The number of total and GFP-positive basal epidermal cells,
697 terminal Schwann cells and other dermal cells at the upper-bulge were counted with
698 reference to GFP, keratin-14, nestin and DAPI staining using Imaris software. Twenty-one
699 zigzag hair follicles from three mice were used. The total number of cells counted were
700 1,010 basal epidermal stem cells, 91 terminal Schwann cells and 319 other dermal cells.
701 To investigate the expression of *Egfl6* in sensory nerves of lanceolate complexes,
702 we examined the GFP expression in the adult thoracic dorsal root ganglia (DRGs) of *Egfl6*-
703 H2BeGFP mice since the nuclei of skin sensory nerves are located in the DRGs. DRGs were
704 isolated and fixed with 4% PFA for 1 hr at 4ºC. Whole DRG tissues were immunostained
705 for βIII tubulin (marker for DRG neurons) and GFP, with DAPI counter stain. Single
706 sectional plane images were obtained as described above. Twenty-five DRGs from three
707 mice were examined and 2,138 DRG neurons were quantified for their nuclear GFP
708 expression.
709 To quantify the expression level of αv integrins, we stained telogen adult dorsal skin
710 of wild-type and *Egfl6* knockout mice for EGFL6, αv integrin and nestin, with DAPI
711 counter stain. Signal intensity of αv integrins at the outer surface of the lanceolate

bioRxiv preprint doi: https://doi.org/10.1101/353490; this version posted June 22, 2018. The copyright holder for this preprint (which was not certified by peer review) is the author/funder, who has granted bioRxiv a license to display the preprint in perpetuity. It is made available under aCC-BY 4.0 International license.

712 complexes was measured using Fiji ImageJ 1.0. Thirteen hair follicles from three wild-type
713 mice and 16 hair follicles from three *Egfl6* knockout mice were used for quantification.
714
715 **_Ex vivo_ skin–nerve preparations**
716 Receptive properties of cutaneous Aδ-LTMRs were studied using mouse hindlimb skin–
717 saphenous nerve preparations *ex vivo* (Zimmermann et al., 2009). Ten- to twelve-week-old
718 male mice, which were in the resting hair growth phase, were euthanized by inhalation of
719 CO_2 gas and the preparations were quickly isolated from the left hindlimb. The excised skin
720 was oriented with the dermis side up in the test chamber and affixed with pins. The
721 preparation was maintained at 32 ± 0.3ºC (pH 7.4) during the experiment under superfusion
722 with modified Krebs-Henseleit solution (Krebs solution), which contained 110.9 mM NaCl,
723 4.7 mM KCl, 2.5 mM $CaCl_2$, 1.2 mM $MgSO_4$, 1.2 mM KH_2PO_4, 25 mM $NaHCO_3$ and 20
724 mM glucose. The perfusate was continuously bubbled and equilibrated with a gas mixture
725 of 95% O_2 and 5% CO_2. The hindlimb skin of mouse is thinner than dorsal skin.
726
727 **Recordings of Aδ-LTMRs**
728 Single Aδ-LTMR was searched and identified when it fulfilled the following criteria: 1)
729 fibers with conduction velocity between 2-10 m/s, 2) fibers responding well to innocuous
730 touch stimulus applied by a blunt glass rod compared to noxious vertical indentation of the
731 skin (compression), 3) fibers without mechanical stimulus intensity-dependent increase in
732 the firing rate, 4) fibers exhibiting a brisk, rapidly adapting discharge at the onset of a
733 supramaximal constant force stimulus (Koltzenburg, Stucky, & Lewin, 1997), 5) fibers not
734 responding to noxious heat and cold stimuli (Figure 3–figure supplement 2) (Zimmermann
735 et al., 2009), and 6) fibers showing a stronger excitation typically in the ramp phase of
736 mechanical stimulation when the stimulus probe was horizontally moving compared to the

bioRxiv preprint doi: https://doi.org/10.1101/353490; this version posted June 22, 2018. The copyright holder for this preprint (which was not certified by peer review) is the author/funder, who has granted bioRxiv a license to display the preprint in perpetuity. It is made available under aCC-BY 4.0 International license.

hold phase, as shown in Figure 3–figure supplement 2. The fibers identified by these criteria in wild type dermis-up skin-nerve preparation exhibited von Frey Hair threshold (vFH) values of ≤0.51–3.23 mN (median: 1.3 mN, IQR: 0.8–2.0 mN) (Figure 3D), which fell into the range of previously reported vFH threshold values of Aδ-LTMRs (or D-hair) with the same dermis-up method (<1–5.7 mN), but not that of high-threshold Aδ-mechano nociceptors (5.7–128 mN) (Zimmermann et al., 2009).

When an Aδ-LTMR was identified, the receptive field (RF) was stimulated with electronic pulses via a bipolar stimulating electrode (frequency of 0.5 Hz, pulse duration of 100 μs and stimulus intensity of <50 V) to measure the conduction velocity of a fiber. The conduction velocity was calculated from the distance and conduction latency of a spike induced by electrical stimulation of the RF. Spontaneous activity of Aδ-LTMRs was analysed for 20 s just before a series of touch mechanical stimulation. Distribution (size and location) of the RFs was mapped on a standardized chart. The size of the RF was measured by calculating the number of pixels in the RF that was drawn on a chart with Image J software. All of the data were stored in a computer via an A/D converter (Power Lab/16s, ADInstruments) with a sampling frequency of 20 kHz. Action potentials were analysed on a computer with the DAPSYS data acquisition system (http://www.dapsys.net). Quantitative mechanical, cold and heat stimuli were then applied to the identified RF in the following order: 1) ramp-and-hold touch mechanical stimulation, 2) cooled from 32°C to 8°C and 3) heated from 32°C to 50°C.

Mechanical stimulation

At first, the mechanical sensitivity of Aδ-LTMRs was semi-quantitatively analysed using a series of self-made von Frey hairs (VFHs: 0.5-17.6 mN, 0.5 mm in diameter). The strength of the weakest filament that caused a mechanical response was taken as the threshold.

bioRxiv preprint doi: https://doi.org/10.1101/353490; this version posted June 22, 2018. The copyright holder for this preprint (which was not certified by peer review) is the author/funder, who has granted bioRxiv a license to display the preprint in perpetuity. It is made available under aCC-BY 4.0 International license.

For quantitative analysis of the mechanical sensitivity of a fiber, a light touch stimulus was applied using a piezo-controlled micromanipulator (Nanomoter MM3A, Kleindiek Nanotechnik, Reutlingen, Germany). The stimulator had a glass probe with a spherical tip (diameter: 0.5 mm). After placing the probe tip to the most sensitive point on the identified RF, a series of ramp-and-hold touch mechanical stimuli were applied by driving the stimulator with a pre-programed computerized protocol. The tip was moved alternately in rostral and caudal directions with displacement in a progressively increasing manner (4–1280 μm) at a speed of 300 μm/s (Figure 3–figure supplement 2A and C). The holding time was set for 2 s between the rostral and caudal movement of the probe tip.

Since all the Aδ-LTMRs were spontaneously silent at the beginning of the experiment without any intentional stimuli, the mechanical response threshold was defined as the displacement that induced the first discharge during the stimulation protocol. If a fiber showed no action potentials during the course of the protocol, even though it exhibited firing as a result of manual touch with a blunt glass rod, then the mechanical threshold was defined to be 1,280 μm. The magnitude of the touch response was represented by the number of spikes evoked during the rostral or caudal movement of the probe (i.e. ramp phases), but not during holding phases of 2 s without probe movement.

Cold and Heat Stimulation

We applied ramp-shaped thermal stimuli to the RF using a feedback-controlled Peltier device (intercross-2000N, Intercross, Co. Ltd., Japan) with a small probe (diameter: 1 mm). From a baseline temperature of 32°C, the RF was gradually cooled down to 8°C over 40 s or heated up to 50°C over 30 s at a constant rate of 0.6°C/s. Original temperature traces are shown in Figure 3–figure supplement 2B.

bioRxiv preprint doi: https://doi.org/10.1101/353490; this version posted June 22, 2018. The copyright holder for this preprint (which was not certified by peer review) is the author/funder, who has granted bioRxiv a license to display the preprint in perpetuity. It is made available under aCC-BY 4.0 International license.

787 **Preparation of Extracellular Matrix Proteins**

788 FLAG-tagged mouse full-length EGFL6 was purified as described below. 293F cells were
789 transfected with the *Egfl6-flag* expression vector and cultured for 4 days according to the
790 manufacturer's instruction (Invitrogen). The supernatant was collected and incubated with
791 anti-FLAG M2 affinity gel (Sigma) overnight at 4ºC. The FLAG affinity gel was collected
792 in an empty Econo-Column (Bio-Rad) and washed with PBS. Bound protein was eluted
793 with 100 μg/ml FLAG peptide in PBS. The eluted protein solution was dialyzed with PBS.
794 Protein concentration was measured with a Pierce BCA Protein Assay Kit using bovine
795 serum albumin (BSA) as a control. The expression vector of RGE-mutant *Egfl6* was
796 generated using the Toyobo KOD-Plus-Mutagenesis kit (Toyobo). FLAG-tagged mouse
797 full-length nephronectin was purified as described previously (Fujiwara et al., 2011).
798 Human plasma fibronectin (Wako) and laminin-511-E8 (Nippi) were purchased from the
799 companies indicated.
800
801 **Solid-Phase Cell Adhesion Assays**
802 Solid-phase cell adhesion assays were performed as described previously (Fujiwara et al.,
803 2011) with minor modifications. Briefly, 96-well cell culture plates were coated with
804 purified ECM proteins and blocked with 1% heat-denatured BSA. Human primary and
805 cultured cell lines were suspended in serum-free DMEM, plated on the coated plates, and
806 incubated for 30 min in a CO_2 incubator at 37ºC. Attached cells were fixed and stained with
807 0.5% crystal violet in 20% methanol for 15 min. The cell-bound crystal violet was extracted
808 with 1% SDS solution and the absorbance was measured at 595 nm. To inhibit cell adhesion
809 activity of different integrins in cell adhesion assays, integrin function blocking antibodies
810 were added to cell suspension before seeding to the coated wells. The cell suspension with
811 the antibodies was incubated for 20 min and then plated on the coated dishes. The function-

bioRxiv preprint doi: https://doi.org/10.1101/353490; this version posted June 22, 2018. The copyright holder for this preprint (which was not certified by peer review) is the author/funder, who has granted bioRxiv a license to display the preprint in perpetuity. It is made available under aCC-BY 4.0 International license.

812 blocking integrin antibodies used in this study were listed below: integrin α2 (P1E6), α3
813 (P1B5), α5 (P1D6), α6 (GoH3), αv (L230), and β1 (P5D2). P1E6, P1B5, P1D6, and P5D2
814 were purchased from the Developmental Studies Hybridoma Bank of the University of Iowa.
815 GoH3 and L230 were purchased from BioLegend and ATCC, respectively. Cell lines used
816 in the assays were human primary keratinocytes, HEK293, T98G, KG-1-C, SF-TY, NTI-4,
817 HT-1080, K562 and K562-a8.
818
819 **Hair plucking assays**
820 Dorsal hairs of 20-day-old anesthetised BALB/c mice were dyed using a neon orange hair
821 colour cream for 30 min. Mice were maintained till the tip of new growing undyed hairs
822 could be observed at the skin surface under a dissection microscope (P32-35). The dyed
823 long club hairs, but not short emerging undyed new hairs, were plucked using tweezers
824 under anaesthesia in an area of 10 x 15 mm. Three days after club hair plucking (P36-38),
825 dorsal skin tissue samples containing both plucked and unplucked hair follicles were
826 collected and subjected to whole-mount immunostaining. Plucked and unplucked skin areas
827 could be easily distinguished by hair colour: the unplucked area showed dyed orange hair
828 colour and the plucked area showed undyed white hair colour. In skin tissue samples, hair
829 shafts could be identified by their autofluorescence. This allowed us to distinguish plucked
830 and unplucked hair follicles within tissue samples under a confocal microscope. Zigzag hair
831 follicles were selected for the analysis. Hair follicle types were distinguished by the
832 following criteria under light-field illumination of 150 μm-thick tissue sections. Zigzag hair
833 follicles are the most abundant follicle type in adult mouse dorsal skin (~81%) (Driskell,
834 Giangreco, Jensen, Mulder, & Watt, 2009). Growing new zigzag hairs in plucked and
835 unplucked hair follicles have one row of medulla cells and the smallest diameter (9.58 ±
836 0.90 μm, n = 32 hair follicles) at the bulge region in comparison to other hair types. Awl

bioRxiv preprint doi: https://doi.org/10.1101/353490; this version posted June 22, 2018. The copyright holder for this preprint (which was not certified by peer review) is the author/funder, who has granted bioRxiv a license to display the preprint in perpetuity. It is made available under aCC-BY 4.0 International license.

837 and auchene hair follicles together make up ~17% of the dorsal skin hair follicles. Growing
838 awl/auchene hairs in plucked and unplucked hair follicles have more than three rows of
839 medulla cells and have a large hair shaft diameter (15.7 ± 1.95 μm, n = 27 hair follicles) at
840 the bulge region. Guard hair follicles are rare (~1% of the adult dorsal skin hair follicles)
841 and can be clearly identified by their prominent large follicle diameter.
842
843 **Statistical analysis**
844 Statistical parameters including the numbers of samples and replicates, types of statistical
845 analysis and statistical significance are indicated in the Results, Figures and Figure Legends.
846 p values: *$p < 0.05$; **$p < 0.01$; ***$p < 0.001$.
847
848 **Data availability**
849 Fastq files of RNA-seq data have been submitted to NCBI SRA, and these data can be
850 accessed through the BioProject ID: PRJNA342736.
851
852

bioRxiv preprint doi: https://doi.org/10.1101/353490; this version posted June 22, 2018. The copyright holder for this preprint (which was not certified by peer review) is the author/funder, who has granted bioRxiv a license to display the preprint in perpetuity. It is made available under aCC-BY 4.0 International license.

853 **Supplemental Figures and Tables**

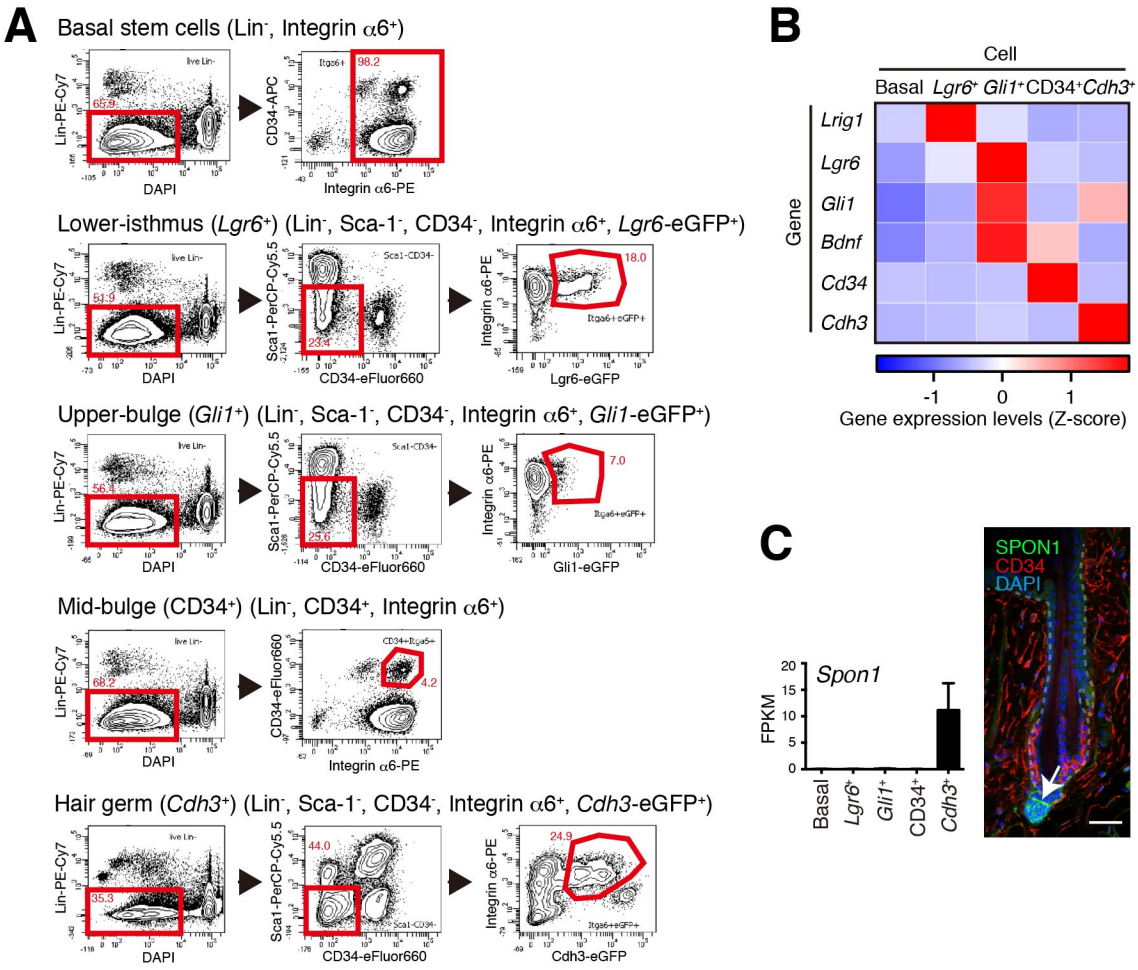

Figure 1–S1 Cheng *et al.*

854

855 **Figure 1–figure supplement 1. FACS-Based Cell Isolation Procedures for Distinct**
856 **Epidermal Stem Cell Populations** (A) FACS sorting procedures of all basal epidermal cell
857 populations using wild-type C57BL/6N mice, *Lgr6*$^+$ lower isthmus epidermal stem cells
858 using *Lgr6-GFP-ires-CreERT2* mice, *Gli1*$^+$ upper-bulge epidermal stem cells using *Gli1-*
859 *eGFP* mice, CD34$^+$ mid-bulge epidermal stem cells using wild-type C57BL/6N mice,
860 *Cdh3*$^+$ hair germ epidermal cells using *Cdh3-eGFP* mice. Gates are indicated by red-line
861 boxes and cells in the gates were further analysed in the next plots or sorted. The numbers
862 in the plots represent the percentage of cells in the gates. Lin$^-$ indicates lineage-negative
863 cells, which are negative for the markers of haematopoietic and endothelial cells (lineage-

bioRxiv preprint doi: https://doi.org/10.1101/353490; this version posted June 22, 2018. The copyright holder for this preprint (which was not certified by peer review) is the author/funder, who has granted bioRxiv a license to display the preprint in perpetuity. It is made available under aCC-BY 4.0 International license.

positive cells). (B) Z-score heat map representing qRT-PCR analysis of sorted cells with compartment-specific gene primers. See Methods for more detail. Data are mean of 3-4 independently isolated biological replicates. (C) Expression levels of *Spon1* gene in different stem cell pools. Immunostaining pattern of SPON1 protein in 8-week-old telogen dorsal hair follicle was shown. White arrow indicates the restricted localization of SPON1 in dermal papilla and the basement membrane between dermal papilla and hair germ. This restricted expression and deposition of SPON1 corroborates little contamination of hair germ cells into the *Gli1*+ upper-bulge population. FPKM, fragments per kilobase of transcript per million mapped reads. Basal, basal epidermal stem cell pool. Data are mean ± SD, n = 3-4. Scale bar, 10 μm.

bioRxiv preprint doi: https://doi.org/10.1101/353490; this version posted June 22, 2018. The copyright holder for this preprint (which was not certified by peer review) is the author/funder, who has granted bioRxiv a license to display the preprint in perpetuity. It is made available under aCC-BY 4.0 International license.

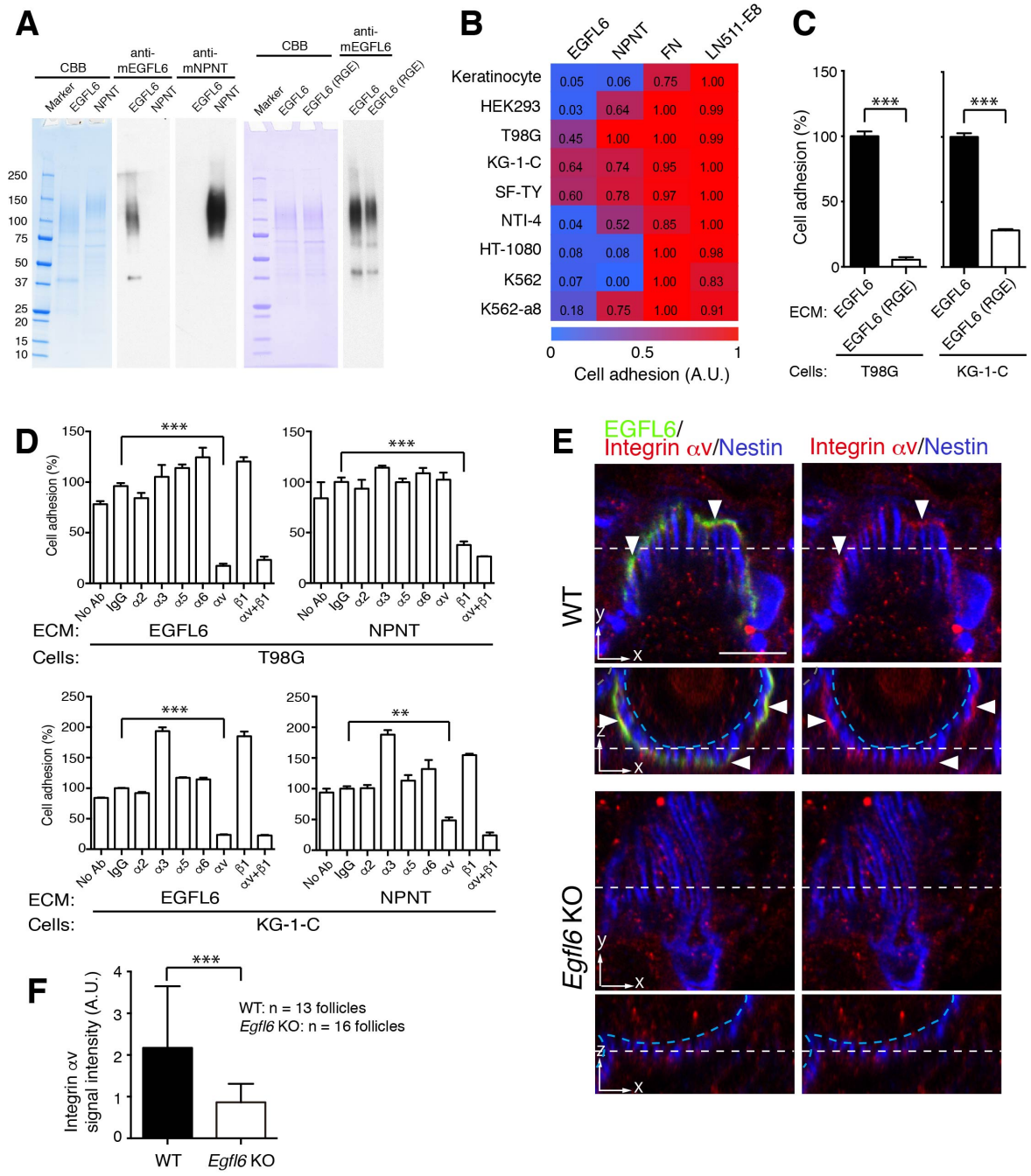

Figure 2–S2 Cheng *et al.*

Figure 2–figure supplement 1. Cell Adhesion to EGFL6 is Mediated by αv Integrins. (A) Coomassie Brilliant Blue (CBB) staining and western blotting of purified EGFL6, RGE-mutant EGFL6, and nephronectin (NPNT) are shown. (B) Heat map display of the results of cell adhesion assays. The number of adhered cells was converted to arbitrary units (A.U.). FN, fibronectin; LN511-E8, laminin-511 E8 fragment. n = 3. Cell lines used are human

bioRxiv preprint doi: https://doi.org/10.1101/353490; this version posted June 22, 2018. The copyright holder for this preprint (which was not certified by peer review) is the author/funder, who has granted bioRxiv a license to display the preprint in perpetuity. It is made available under aCC-BY 4.0 International license.

primary keratinocytes, human embryonic kidney epithelial cell line HEK293, human glioblastoma cell line T98G, Human glioma cell line KG-1-C, human skin fibroblast cell line SF-TY, human embryonic fibroblast cell line NTI-4, human sarcoma cell line HT-1080, human myelogenous leukemia cell line K562 and K562 transfected with human integrin α8 cDNA K562-a8. (C) Cell adhesion assays with T98G and KG-1-C cells plated on EGFL6 or RGE-mutant EGFL6-coated dishes. Data are mean ± SEM, n = 3. (D) Cell adhesion inhibition assays with integrin antibodies. Data are mean ± SEM, n = 3. (E) 8-week-old telogen dorsal HFs of wild-type and *Egfl6* knockout mice were stained for EGFL6, integrin αv and nestin. Scale bar, 10 μm. Blue dashed lines indicate the surface of follicle epidermis and white dashed lines indicate cross-section positions. (F) Quantification of αv integrin signal intensity in lanceolate complexes. Data are mean ± SD. Statistics (C, D, F): two-tailed unpaired *t*-test.

bioRxiv preprint doi: https://doi.org/10.1101/353490; this version posted June 22, 2018. The copyright holder for this preprint (which was not certified by peer review) is the author/funder, who has granted bioRxiv a license to display the preprint in perpetuity. It is made available under aCC-BY 4.0 International license.

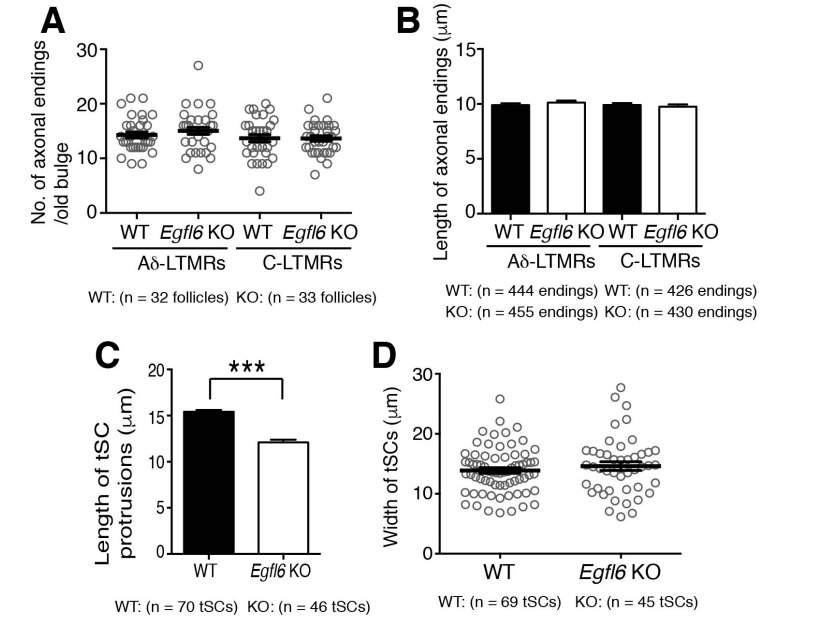

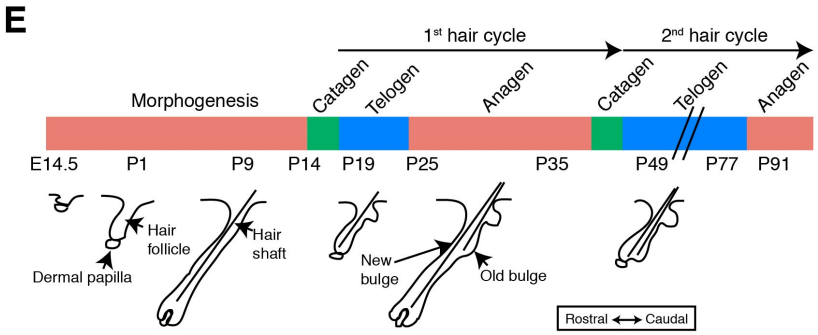

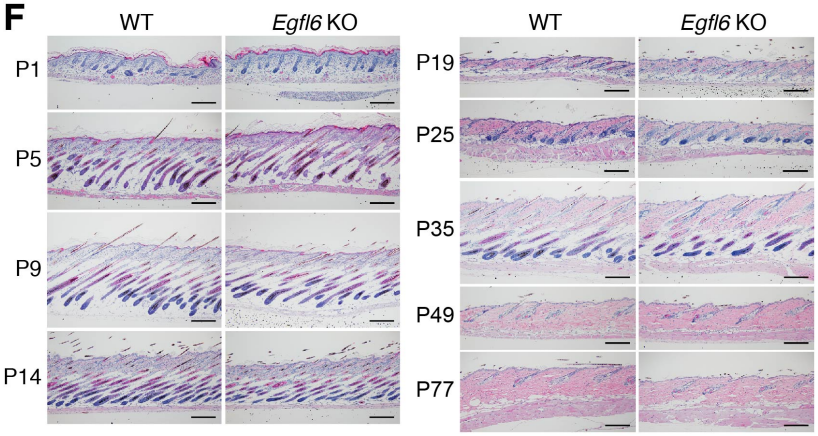

Figure 3–S1 Cheng *et al.*

Figure 3–figure supplement 1. Quantification of Morphological Characteristics of Axonal Endings and tSC Processes and Histological Examination of Skin Tissue Morphology in Wild-type and *Egfl6* Knockout Mice (A) Number of axonal endings in the old bulge of zigzag hair follicles was counted. Data are mean ± SEM, n = 32 hair follicles

bioRxiv preprint doi: https://doi.org/10.1101/353490; this version posted June 22, 2018. The copyright holder for this preprint (which was not certified by peer review) is the author/funder, who has granted bioRxiv a license to display the preprint in perpetuity. It is made available under aCC-BY 4.0 International license.

for wild-type and n = 33 hair follicles for knockout from 3 mice each. (B) Length of axonal endings in the old bulge of zigzag hair follicles was measured. Data are mean ± SEM, n = 444 axonal endings for wild-type and n = 455 axonal endings for knockout from 3 mice each. (C) Length and width of tSC processes were measured. Data are mean ± SEM, n = 70 tSCs for wild-type and n = 46 tSCs for knockout from 3 mice each. (D) Width of tSC processes were measured. Data are mean ± SEM, n = 69 tSCs for wild-type and n = 45 tSCs for knockout from 3 mice each. (E) Schematic representation of mouse hair follicle morphogenesis and the following regeneration cycles. During the first anagen phase (P25-P35), old and new hair bulge structures form. (F) H&E-stained dorsal skin of wild-type and *Egfl6* knockout mice. Scale bars, 100 μm.

bioRxiv preprint doi: https://doi.org/10.1101/353490; this version posted June 22, 2018. The copyright holder for this preprint (which was not certified by peer review) is the author/funder, who has granted bioRxiv a license to display the preprint in perpetuity. It is made available under aCC-BY 4.0 International license.

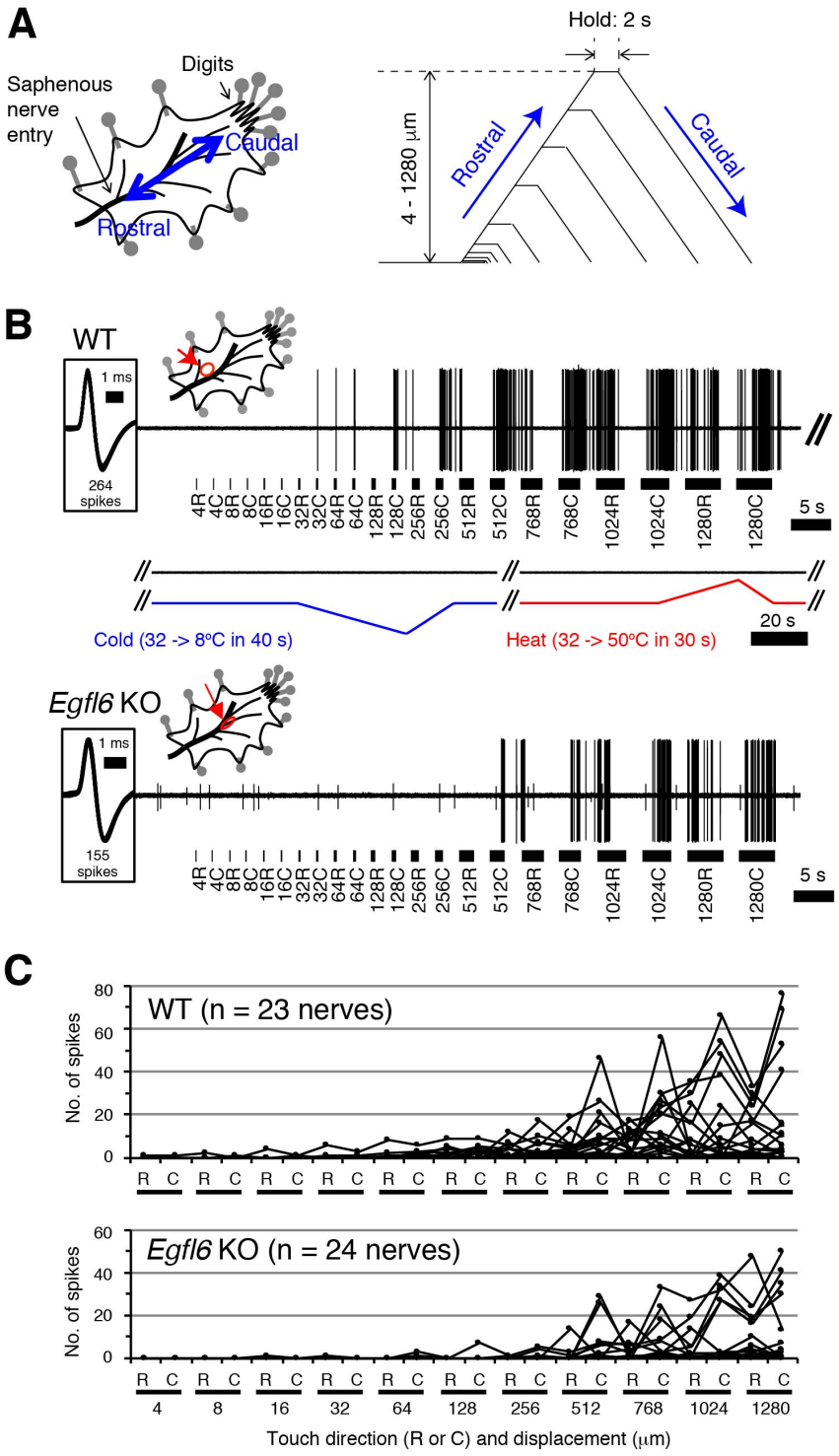

Figure3–S2 Cheng *et al.*

Figure 3–figure supplement 2. Skin–Nerve Preparation and Recordings of Responses of Aδ-LTMRs (A) Mouse skin–nerve preparation *ex vivo*, which is oriented with the dermis side up in the test chamber and affixed with pins. A ramp-and-hold touch stimulus protocol is shown. A probe tip was moved alternately in rostral and caudal directions with

bioRxiv preprint doi: https://doi.org/10.1101/353490; this version posted June 22, 2018. The copyright holder for this preprint (which was not certified by peer review) is the author/funder, who has granted bioRxiv a license to display the preprint in perpetuity. It is made available under aCC-BY 4.0 International license.

displacement in a progressively increasing manner (4–1280 μm) at a speed of 300 μm/s. The holding time was set for 2 s between the rostral and caudal movement of the tip. (B) Representative responses in the wild-type (upper panel) and *Egfl6* knockout skin (lower panel). Note the first spike of the wild-type in response to touch stimulus with caudal displacement of 32 μm (i.e. 32C). No firings were observed in response to cold (from 32ºC to 8ºC in 40 s) or heat (from 32ºC to 50ºC in 30 s) stimulations. In the knockout, smaller responses to touch stimuli can be observed with the higher threshold displacement of 512 μm. Spike shapes are shown in insets squared at the left side. All of the spikes generated during a series of stimuli are superimposed (264 spikes in wild-type, and 155 spikes in knockout). The distribution of receptive fields is indicated by an arrow. (C) Individual response patterns in the wild-type (n = 23, upper panel) and the knockout (n = 24, lower panel).

bioRxiv preprint doi: https://doi.org/10.1101/353490; this version posted June 22, 2018. The copyright holder for this preprint (which was not certified by peer review) is the author/funder, who has granted bioRxiv a license to display the preprint in perpetuity. It is made available under aCC-BY 4.0 International license.

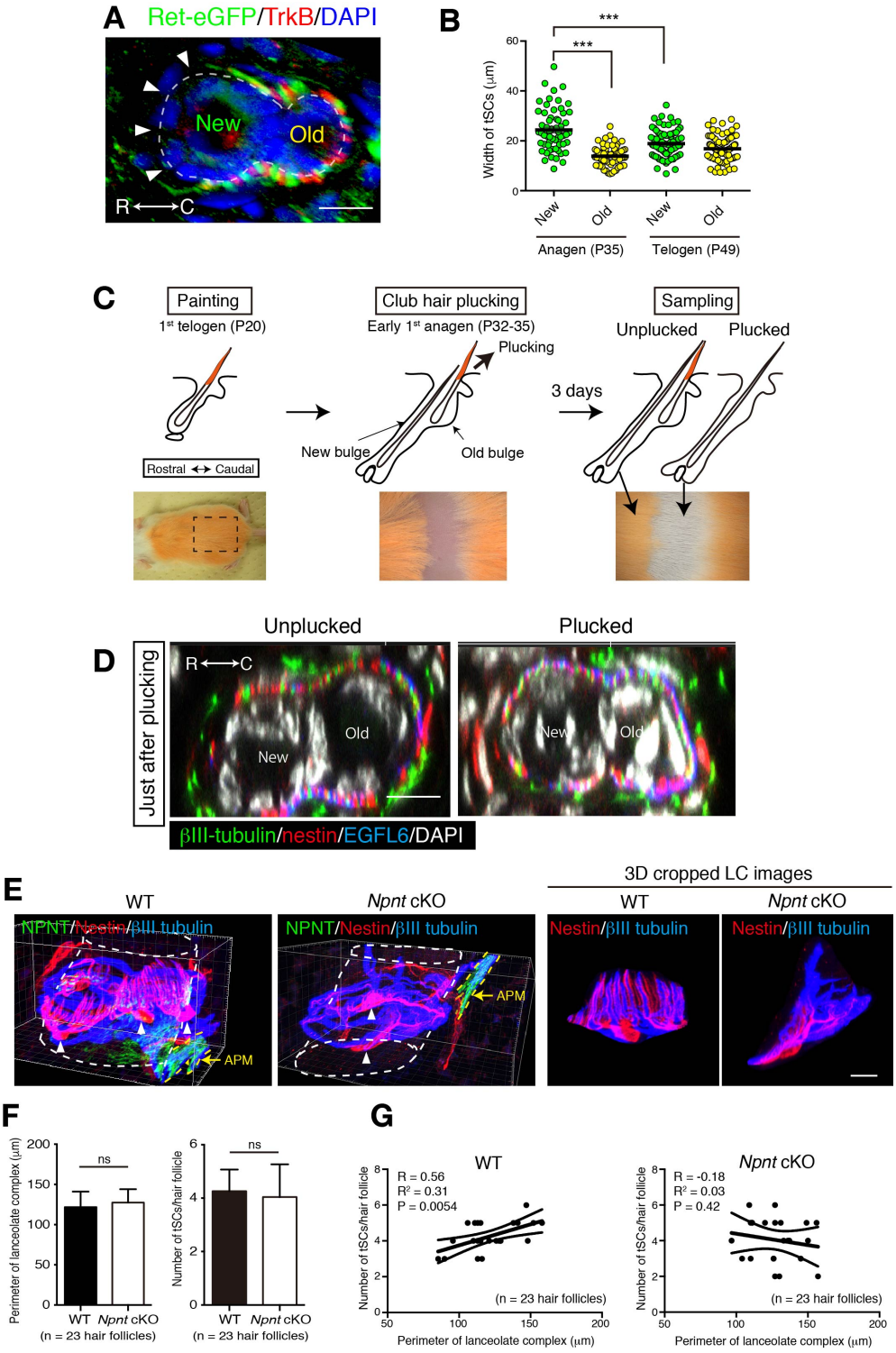

Figure 4–S1 Cheng *et al.*

Figure 4–figure supplement 1. The old bulge formation provides stable epidermal-neuronal interfaces (A) A cross-sectional view of 7-week-old telogen upper bulge stained for *Ret*-eGFP, TrkB and DAPI. Closed arrowheads indicate a gap of lanceolate endings. (B) The width of tSCs in new and old bulges in the first anagen (P35) and second telogen (P49)

bioRxiv preprint doi: https://doi.org/10.1101/353490; this version posted June 22, 2018. The copyright holder for this preprint (which was not certified by peer review) is the author/funder, who has granted bioRxiv a license to display the preprint in perpetuity. It is made available under aCC-BY 4.0 International license.

936 follicles were quantified. n = 60–92 tSCs from 3 mice. Individual measurement data are
937 shown as circles. Mean ± SEM are shown as bars, n = 3 mice. Statistical comparisons were
938 performed using two-tailed unpaired *t*-test. (C) Procedure of club hair plucking experiments.
939 (D) Transverse sectional views of upper-bulge with club-hair unplucked and plucked P32
940 early anagen hair follicles stained for βIII-tubulin, nestin, EGFL6 and DAPI. Just after
941 plucking, little structural damage to the old bulge epidermis and LCs were observed. (E) 3D
942 reconstituted immunostaining images of upper-bulge region of 7-week-old telogen
943 Awl/auchene hair follicles of wild-type and epidermis-specific conditional nephronectin
944 (*Npnt*) knockout mice (Keratin5-Cre/Npnt fl/fl). Upon epidermal deletion of *Npnt* gene,
945 arrector pili muscles (APM) moved above the bulge (Fujiwara et al., 2011), where LCs were
946 located. Arrowheads indicate the nuclei of tSCs. In the mutant, some hair follicles showed
947 disrupted patterning of longitudinal sensory nerve endings and tSCs processes. This mutant
948 image shows a significantly fewer number of longitudinal lanceolate endings and tSC
949 processes (see also 3D cropped LC images). (F) The perimeter and number of LCs in
950 randomly selected non-guard hair follicles of wild-type and *Npnt* conditional knockout mice
951 were measured. No statistically significant difference was observed. Data are mean ± SD, n
952 = 23 hair follicles from wild-type and mutant mice, respectively. (G) The number of tSCs
953 were plotted against the perimeter of LCs. In the wild-type, the number of tSCs correlated
954 well with the perimeter of LCs, *i.e.* perimeter of hair follicles, while in the *Npnt* knockout
955 mice, distribution of the values of "number of tSC/perimeter of LCs" was scattered and their
956 correlation was lost (see R^2 and p-value), indicating the anatomical changes of LCs in *Npnt*
957 mutants. n = 23 hair follicles from wild-type and mutant mice, respectively. Scale bars, 10
958 μm.
959
960

bioRxiv preprint doi: https://doi.org/10.1101/353490; this version posted June 22, 2018. The copyright holder for this preprint (which was not certified by peer review) is the author/funder, who has granted bioRxiv a license to display the preprint in perpetuity. It is made available under aCC-BY 4.0 International license.

961 **Figure 1– table supplement 1. Normalized Enrichment Score (NES) of Gene Set**

962 **Enrichment Analysis (GSEA)**

Cdh3	CD34	Lgr6	Gli1	GO terms
1.674	0.916	-0.868	1.210	NEGATIVE_REGULATION_OF_TRANSCRIPTION_DNA_DEPENDENT
1.662	0.899	-0.859	1.204	REGULATION_OF_TRANSCRIPTION_FROM_RNA_POLYMERASE_II_PROMOTER
1.655	0.930	-0.808	1.201	POSITIVE_REGULATION_OF_NUCLEOBASENUCLEOSIDENUCLEOTIDE_AND_NUCLEIC_ACID_METABOLIC_PROCESS
1.639	0.907	-0.863	1.186	NEGATIVE_REGULATION_OF_RNA_METABOLIC_PROCESS
1.571	0.981	-0.898	1.228	NEGATIVE_REGULATION_OF_NUCLEOBASENUCLEOSIDENUCLEOTIDE_AND_NUCLEIC_ACID_METABOLIC_PROCESS
1.591	0.989	-0.862	1.167	POSITIVE_REGULATION_OF_TRANSCRIPTION
1.561	0.928	-0.817	1.148	POSITIVE_REGULATION_OF_RNA_METABOLIC_PROCESS
1.552	0.928	-0.823	1.145	POSITIVE_REGULATION_OF_TRANSCRIPTIONDNA_DEPENDENT
1.492	0.990	-0.850	1.252	NEGATIVE_REGULATION_OF_METABOLIC_PROCESS
1.474	1.000	-0.854	1.249	NEGATIVE_REGULATION_OF_CELLULAR_METABOLIC_PROCESS
1.507	0.921	0.860	1.260	NEGATIVE_REGULATION_OF_TRANSCRIPTION_FROM_RNA_POLYMERASE_II_PROMOTER
1.508	1.006	0.897	1.099	TRANSMEMBRANE_RECEPTOR_PROTEIN_TYROSINE_KINASE_SIGNALING_PATHWAY
1.688	-0.999	-0.902	1.191	REGULATION_OF_RNA_METABOLIC_PROCESS
1.652	-0.988	-0.896	1.187	REGULATION_OF_TRANSCRIPTIONDNA_DEPENDENT
1.666	-0.918	-0.864	1.253	REGULATION_OF_TRANSCRIPTION
1.616	-0.969	-0.914	1.192	REGULATION_OF_NUCLEOBASENUCLEOSIDENUCLEOTIDE_AND_NUCLEIC_ACID_METABOLIC_PROCESS
1.510	-0.938	-0.885	1.134	POSITIVE_REGULATION_OF_METABOLIC_PROCESS
1.496	-0.939	-0.911	1.122	POSITIVE_REGULATION_OF_CELLULAR_METABOLIC_PROCESS
1.503	-1.349	-1.005	1.305	MULTI_ORGANISM_PROCESS

bioRxiv preprint doi: https://doi.org/10.1101/353490; this version posted June 22, 2018. The copyright holder for this preprint (which was not certified by peer review) is the author/funder, who has granted bioRxiv a license to display the preprint in perpetuity. It is made available under aCC-BY 4.0 International license.

1.568	-0.953	0.965	1.224	TRANSCRIPTION_FROM_RNA_POLYMERASE_II_PROMOTER
1.537	-1.115	0.972	1.195	PROTEIN_KINASE_CASCADE
1.604	-0.901	0.988	1.234	PROTEIN_AMINO_ACID_PHOSPHORYLATION
1.551	-1.108	1.041	1.316	REGULATION_OF_MAP_KINASE_ACTIVITY
1.665	-0.999	1.095	1.032	FEEDING_BEHAVIOR
1.629	-0.837	1.165	1.424	MAPKKK_CASCADE
1.473	-1.314	1.197	1.330	RESPONSE_TO_BIOTIC_STIMULUS
1.818	1.208	-0.932	1.375	MUSCLE_DEVELOPMENT
1.715	1.316	-1.093	1.341	ENZYME_LINKED_RECEPTOR_PROTEIN_SIGNALING_PATHWAY
1.544	1.286	-1.377	1.332	TRANSMEMBRANE_RECEPTOR_PROTEIN_SERINE_THREONINE_KINASE_SIGNALING_PATHWAY
1.700	1.052	0.824	1.335	NEGATIVE_REGULATION_OF_TRANSCRIPTION
1.624	1.093	0.835	1.186	POSITIVE_REGULATION_OF_TRANSCRIPTION_FROM_RNA_POLYMERASE_II_PROMOTER
1.623	1.231	-1.321	1.039	FEMALE_PREGNANCY
1.390	-1.241	-0.947	0.995	REGULATION_OF_KINASE_ACTIVITY
1.385	-1.198	-1.146	0.998	G_PROTEIN_COUPLED_RECEPTOR_PROTEIN_SIGNALING_PATHWAY
1.379	-1.250	-0.898	0.994	REGULATION_OF_TRANSFERASE_ACTIVITY
1.338	-1.188	-0.889	1.047	REGULATION_OF_MOLECULAR_FUNCTION
1.449	-1.128	-0.957	1.055	REGULATION_OF_SIGNAL_TRANSDUCTION
1.446	-1.213	-0.911	1.033	REGULATION_OF_PROTEIN_KINASE_ACTIVITY
1.301	-1.199	-0.998	1.278	CELL_PROLIFERATION
1.466	-1.023	1.053	1.219	PHOSPHORYLATION
1.417	-1.100	0.979	1.203	POST_TRANSLATIONAL_PROTEIN_MODIFICATION
1.425	-0.968	1.021	1.091	SECOND_MESSENGER_MEDIATED_SIGNALING
1.275	-1.170	1.081	1.087	REGULATION_OF_DEVELOPMENTAL_PROCESS
1.523	-1.081	-1.118	0.774	NUCLEOCYTOPLASMIC_TRANSPORT
1.516	-1.095	-1.097	0.759	NUCLEAR_TRANSPORT
1.555	-1.082	-1.215	0.785	NUCLEAR_IMPORT
1.629	-1.056	-1.234	0.804	PROTEIN_IMPORT_INTO_NUCLEUS
1.618	-1.180	0.850	0.915	B_CELL_ACTIVATION
1.514	0.913	-0.943	0.933	STRIATED_MUSCLE_DEVELOPMENT
1.213	-1.495	1.241	1.433	RESPONSE_TO_WOUNDING

bioRxiv preprint doi: https://doi.org/10.1101/353490; this version posted June 22, 2018. The copyright holder for this preprint (which was not certified by peer review) is the author/funder, who has granted bioRxiv a license to display the preprint in perpetuity. It is made available under aCC-BY 4.0 International license.

1.303	-1.510	1.144	1.365	RESPONSE_TO_EXTERNAL_STIMULUS
1.304	-1.822	1.296	1.300	DEFENSE_RESPONSE
1.384	-1.278	1.255	1.621	DETECTION_OF_EXTERNAL_STIMULUS
1.211	-1.096	1.146	1.599	GROWTH
1.139	-1.151	0.978	1.487	CATION_HOMEOSTASIS
1.205	1.116	1.222	1.631	NEURON_DIFFERENTIATION
1.152	1.097	1.242	1.577	NEURON_DEVELOPMENT
1.159	1.075	1.114	1.537	GENERATION_OF_NEURONS
1.023	1.012	1.089	1.520	NEUROGENESIS
1.233	1.168	0.943	1.375	NERVOUS_SYSTEM_DEVELOPMENT
1.605	1.198	1.168	1.634	GLUTAMATE_SIGNALING_PATHWAY
1.461	1.090	1.112	1.654	BRAIN_DEVELOPMENT
1.450	1.273	0.969	1.585	ORGAN_MORPHOGENESIS
1.603	1.140	1.287	1.360	CYCLIC_NUCLEOTIDE_MEDIATED_SIGNALING
1.487	1.102	1.180	1.412	CELL_CELL_SIGNALING
1.624	1.024	1.160	1.300	G_PROTEIN_SIGNALING_COUPLED_TO_CYCLIC_NUCLEOTIDE_SECOND_MESSENGER
1.162	-0.900	1.621	1.517	SODIUM_ION_TRANSPORT
1.081	-1.806	1.593	1.514	DEFENSE_RESPONSE_TO_BACTERIUM
1.261	-1.316	1.669	1.552	METAL_ION_TRANSPORT
1.251	-1.175	1.430	1.604	TISSUE_DEVELOPMENT
1.083	1.052	1.476	1.761	DEVELOPMENTAL_MATURATION
1.055	1.061	1.603	1.492	MONOVALENT_INORGANIC_CATION_TRANSPORT
1.022	-1.147	1.529	1.558	ECTODERM_DEVELOPMENT
0.957	-1.205	1.505	1.554	EPIDERMIS_DEVELOPMENT
-0.800	-1.495	1.683	1.511	KERATINOCYTE_DIFFERENTIATION
-0.693	-0.899	1.608	1.414	REGULATION_OF_DEFENSE_RESPONSE
-1.175	-0.977	1.651	1.799	SYNAPTOGENESIS
-1.526	-1.289	1.591	1.748	SYNAPSE_ORGANIZATION_AND_BIOGENESIS
-0.849	0.874	1.491	1.286	ALCOHOL_METABOLIC_PROCESS
-1.015	-1.208	1.454	1.344	CATION_TRANSPORT
-1.170	-1.286	1.437	1.190	LIPID_METABOLIC_PROCESS
-1.047	-1.143	1.345	1.164	CELLULAR_LIPID_METABOLIC_PROCESS
-0.947	-1.732	1.647	1.132	INNATE_IMMUNE_RESPONSE
1.501	1.102	1.530	1.662	EXCRETION
1.521	-1.415	1.419	1.633	DETECTION_OF_STIMULUS
1.663	-1.418	1.902	1.663	CALCIUM_INDEPENDENT_CELL_CELL_ADHESION
1.497	1.355	1.321	1.673	CELL_MATURATION

bioRxiv preprint doi: https://doi.org/10.1101/353490; this version posted June 22, 2018. The copyright holder for this preprint (which was not certified by peer review) is the author/funder, who has granted bioRxiv a license to display the preprint in perpetuity. It is made available under aCC-BY 4.0 International license.

1.465	1.344	1.219	1.599	ANATOMICAL_STRUCTURE_MORPHOGENESIS
1.711	1.409	1.291	1.590	PATTERN_SPECIFICATION_PROCESS
1.388	1.539	1.376	1.665	POTASSIUM_ION_TRANSPORT
1.609	1.805	1.517	1.718	AXON_GUIDANCE
1.899	1.849	-0.724	1.802	DETECTION_OF_ABIOTIC_STIMULUS
1.870	1.802	-0.720	1.725	DETECTION_OF_STIMULUS_INVOLVED_IN_SENSORY_PERCEPTION
1.576	1.753	-0.730	1.556	HORMONE_SECRETION
1.695	1.504	-1.197	1.495	SKELETAL_DEVELOPMENT
1.867	1.718	1.092	1.274	MESODERM_DEVELOPMENT
0.875	1.736	0.825	1.504	REGULATION_OF_HEART_CONTRACTION
0.909	1.959	-1.410	1.177	GENERATION_OF_A_SIGNAL_INVOLVED_IN_CELL_CELL_SIGNALING

963

964

bioRxiv preprint doi: https://doi.org/10.1101/353490; this version posted June 22, 2018. The copyright holder for this preprint (which was not certified by peer review) is the author/funder, who has granted bioRxiv a license to display the preprint in perpetuity. It is made available under aCC-BY 4.0 International license.

965 **Figure 2–table supplement 1. List of ECM proteins screened for upper-bulge**

966 **localization with immunohistochemical analysis**

Gene symbol	Protein name (Abbreviation)	Antibody ID	Manufacturer	Upper-bulge localization	Tissue localization
Aspn	Asporin	ab58741	abcam	Yes	Upper bulge sensory neuron
Crispld1	Cysteine-rich secretory protein LCCL domain containing 1 (CRISPLD1)	ab123039	abcam	Yes	Basement membrane zone of upper-bulge
Epdr1	Ependymin related protein 1 (EPDR1)	PA283664	Cusabio	No	Uncertain
Col5a2	Collagen, type V, alpha 2 (COL5A2)	ab7046	abcam	Yes	Broadly distributed in the epidermal-dermal basement membrane zone
Vwa2	von Willebrand factor A domain-containing protein 2 (VWA2)	ab111164	abcam	No	Follicle-arrector pili muscle junction
Fam101b	Refilin B	orb183474	biorbyt	No	Uncertain
Ltbp1	Latent TGF-beta-binding protein 1 (LTBP1)	PA807018	Cusabio	No	Uncertain
Postn	Periostin	ab14041	abcam	Yes	Basement membrane zone of upper-and mid-bulge
Spon2	Spondin-2	PA006509	Cusabio	No	Uncertain
Egfl6	Epidermal growth factor-like protein 6 (EGFL6)	CUK1203	Fujiwara lab (in house)	Yes	Upper-bulge collar matrix
Igfbp5	Insulin-like growth factor binding protein 5 (IGFBP5)	AF578	R&D	Yes	Upper bulge sensory neuron
Col8a2	Collagen, type VIII, alpha 2 (COL8A2)	34099	USBiological	No	Uncertain
Igfbp7	Insulin-like growth factor binding protein 7 (IGFBP7)	ab129302	abcam	No	Uncertain
Adamtsl4	ADAMTS-like 4 (ADAMTSL4)			Not tested	
Col4a3	Collagen, type IV, alpha 3 (COL4A3)	H31	Shigei Med. Res. Inst.	Yes	Basement membrane zone of upper-bulge
Col4a4	Collagen, type IV, alpha 4 (COL4A4)	RH42	Shigei Med. Res. Inst.	Yes	Basement membrane zone of upper-bulge

967
968
969

bioRxiv preprint doi: https://doi.org/10.1101/353490; this version posted June 22, 2018. The copyright holder for this preprint (which was not certified by peer review) is the author/funder, who has granted bioRxiv a license to display the preprint in perpetuity. It is made available under aCC-BY 4.0 International license.

970 **Figure 3–table supplement 1. General characteristics of Aδ-LTMRs**

Outcomes	WT (n=23 nerves)	*Egfl6* KO (n=24 nerves)	*p* value
Activation threshold (V)	3.0 (2.0-4.0)	3.0 (2.0-6.0)	$p = 0.778$
Conduction velocity (m/s)	6.6 (5.1-7.7)	7.7 (5.0-8.6)	$p = 0.115$
Spontaneous activity (imp/s)	0 (0-0)	0 (0-0)	$p > 0.999$
Receptive field size (mm^2)	6.5 (4.7-13.2)	4.8 (2.8-7.3)	$p = 0.059$

971

972

bioRxiv preprint doi: https://doi.org/10.1101/353490; this version posted June 22, 2018. The copyright holder for this preprint (which was not certified by peer review) is the author/funder, who has granted bioRxiv a license to display the preprint in perpetuity. It is made available under aCC-BY 4.0 International license.

973 **Table 1. Antibodies used in this study**

ANTIBODY	SOURCE	IDENTIFIER
Rabbit anti-mouse EGFL6	Fujiwara Lab	This paper
Rabbit anti-mouse nephronectin	Fujiwara Lab	This paper
Mouse anti-keratin 14	abcam	LL002 (ab77684)
Mouse anti-keratin 15	Santa Cruz	LHK15 (sc-47697)
Mouse anti-βIII-tubulin	abcam	2G10 (ab78078)
Chicken anti-nestin	Aves Labs	NES0407
Rat anti-nestin	Millipore	rat-401 (MAB353)
Chicken anti-GFP	abcam	ab13970
Rabbit anti-GFP	MBL	598
Mouse anti-laminin γ1	Millopore	MAB1914
Rat anti-integrin αv	abcam	RMV-7
Goat anti-TrkB	R&D Systems	AF1494
Rat anti-CD45-PE-Cy7	eBioscience	30-F11
Rat anti-TER-119-PE-Cy7	eBioscience	TER119
Rat anti-CD31-PE-Cy7	eBioscience	390
Rat anti-Sca-1-PerCP-Cy5.5	eBioscience	D7
Rat anti-CD34-eFluor660	eBioscience	RAM34
Rat anti-CD49f-PE	eBioscience	GoH3
Mouse anti-integrin α2	DSHB	P1E6
Mouse anti-integrin α3	DSHB	P1B5
Mouse anti-integrin α5	DSHB	P1D6
Rat anti-integrin α6	BioLegend	GoH3 (313614)
Mouse anti-integrin αv	ATCC	L230
Mouse anti-integrin β1	DSHB	P5D2

974

975

976

bioRxiv preprint doi: https://doi.org/10.1101/353490; this version posted June 22, 2018. The copyright holder for this preprint (which was not certified by peer review) is the author/funder, who has granted bioRxiv a license to display the preprint in perpetuity. It is made available under aCC-BY 4.0 International license.

977 **Table 2. Primer sequences for qRT-PCR**

Target genes	**Primer sequences**
Gapdh (Forward)	TGCCAGCCTCGTCCCGTAG
Gapdh (Reverse)	CGGCCTTGACTGTGCCGTTG
Lrig1 (Forward)	TGTGTGTCTGAGAGACCCGAGC
Lrig1 (Reverse)	CAGAGCCACTGTGTGCTGTTGT
Lgr6 (Forward)	GGCTCCGAATCCTGGAGCTGT
Lgr6 (Reverse)	CTCAGGGTGGATGGCACGGA
Gli1 (Forward)	ATCTCCGGGCGGTTCCTACG
Gli1 (Reverse)	TGACTTCAGCTGGCAGGTTGC
Bdnf (Forward)	GCGGCGCCCATGAAAGAAGT
Bdnf (Reverse)	GGCCGAACCTTCTGGTCCTCA
Cd34 (Forward)	TGGCGCTGGGTAGCTCTCTG
Cd34 (Reverse)	TAGTCTCTGAGATGGCTGGTGTGG
Cdh3 (Forward)	TGGGGAAAGTAGCCTTGGCTGG
Cdh3 (Reverse)	CAGCCTCTGAGGGAAGGGACC

978

979

bioRxiv preprint doi: https://doi.org/10.1101/353490; this version posted June 22, 2018. The copyright holder for this preprint (which was not certified by peer review) is the author/funder, who has granted bioRxiv a license to display the preprint in perpetuity. It is made available under aCC-BY 4.0 International license.

980 **Table 3. RNA-seq read counts and mapping statistics**

	Raw Read Count	Trimmed Read Count	rDNA Read Count	Multi-Mapped Read Count	Uniquely Mapped Read Count
Mouse_Basal_ Cells_Rep1	11,757,494	11,278,061	148,700	170,077	10,456,332
Mouse_Basal_ Cells_Rep2	11,245,045	10,668,752	73,729	134,777	10,051,376
Mouse_Basal_ Cells_Rep3	11,313,239	10,747,103	108,596	146,602	10,089,518
Mouse_Bulge_ StemCells_Rep1	11,735,034	11,181,377	64,614	183,557	10,520,864
Mouse_Bulge_ StemCells_Rep2	11,917,049	11,515,851	54,154	175,176	10,889,932
Mouse_Bulge_ StemCells_Rep3	13,417,100	12,895,113	88,655	218,495	12,090,872
Mouse_Cdh3+_ Cells_Rep1	10,875,593	10,409,342	68,193	177,407	9,574,901
Mouse_Cdh3+_ Cells_Rep2	11,565,616	10,993,093	65,001	185,981	10,079,620
Mouse_Cdh3+_ Cells_Rep3	11,405,265	10,746,768	76,143	206,384	9,790,096
Mouse_Cdh3+_ Cells_Rep4	11,759,881	11,186,543	85,902	191,154	10,274,371
Mouse_Gli1+_ Cells_Rep1	12,063,488	11,478,537	57,630	178,646	10,751,521
Mouse_Gli1+_ Cells_Rep2	19,762,234	18,804,713	178,685	303,848	17,446,776
Mouse_Gli1+_ Cells_Rep3	19,543,117	18,568,695	122,017	287,214	17,378,904
Mouse_Lgr6+_ Cells_Rep1	20,044,455	19,058,807	121,507	307,804	17,798,594
Mouse_Lgr6+_ Cells_Rep2	19,756,354	18,736,071	197,458	298,652	17,386,391
Mouse_Lgr6+_ Cells_Rep3	19,639,299	18,680,969	217,502	298,146	17,210,635

981

982

983